Principles and approaches for the machining simulation of ceramic matrix composites at microscale: a review and outlook

Simon Unseld, Ralf Goller, Dietmar Koch

Angaben zur Veröffentlichung / Publication details:

Unseld, Simon, Ralf Goller, and Dietmar Koch. 2023. "Principles and approaches for the machining simulation of ceramic matrix composites at microscale: a review and outlook." *Open Ceramics* 16 (September): 100454. https://doi.org/10.1016/j.oceram.2023.100454.

Open Ceramics 16 (2023) 100454

Contents lists available at ScienceDirect

Open Ceramics

journal homepage: www.sciencedirect.com/journal/open-ceramics

Principles and approaches for the machining simulation of ceramic matrix composites at microscale: A review and outlook

Simon Unseld [a,*], Ralf Goller [a], Dietmar Koch [b]

[a] Technical University of Applied Sciences Augsburg, Germany
[b] Institute of Materials Resource Management, University of Augsburg, Germany

ARTICLE INFO

Handling Editor: Dr P Colombo

Keywords:
Machining simulation
Ceramic matrix composite
Brittle material model
Microscale
Cohesive zone model

ABSTRACT

Ceramic Matrix Composites (CMC) are advanced materials composed of ceramic fibers embedded in a ceramic matrix, resulting in a highly durable and lightweight composite structure offering exceptional high-temperature performance, excellent mechanical properties, and superior resistance to wear and corrosion. CMC find applications in industries such as aerospace, automotive, energy, and defense, where high strength and thermal stability are crucial. Despite their numerous advantages, machining CMC presents unique challenges. The hardness and brittleness of ceramics make them difficult to machine using conventional methods. The abrasive nature of ceramic particles can rapidly wear down cutting tools, leading to decreased tool life and increased costs. Numeric simulations for the machining of CMC are therefore particularly interesting due to their ability to provide insights into tool-material interactions and optimize machining parameters without the need for expensive and time-consuming physical trials. This paper discusses existing methods and approaches from different materials like Carbon Fiber Reinforced Plastics (CFRP) and monolithic ceramics and puts forward an outlook for the numerical simulation of the machining process of CMC.

1. Introduction

The machining of brittle materials like ceramics, glasses, bones and composites such as carbon fiber reinforced plastics (CFRP) and ceramic matrix composites (CMC) is already an established part of the process chain in industrial sectors such as aerospace, automotive and medical engineering. Compared to ductile metallic materials, one of the challenges in machining brittle materials lies in the rapid and sometimes seemingly random crack propagation in the material. These cracks form with the initial contact between the tool and the material and extending throughout the entire machining process. Such behavior makes both a generalized theoretical description of the material's behavior and the investigation of different factors influencing the machining process more difficult. So far, many publications have addressed the numerical simulation of the machining process or experimental tests to gain insight into the material-specific crack propagation behavior and predict damage more precisely [1,2].

Compared to existing reviews in the field of machining simulation of CFRP [3–10] and ceramics and other brittle materials [11–16], this review paper is based on the combination of individual state of the art approaches of different materials, which are transferred to the new field of machining simulation of CMCs. Thereby, the currently still deficient availability of data by existing approaches from different disciplines shall be transferred and applied. In this paper, fundamentals will be given, and different research of recent years will be presented. Thereby the focus lies on the main aspect of microstructural modeling, while other topics like meso- and macroscale approaches are deliberately excluded. For a more detailed investigation of these topics, please refer to the comprehensive literature mentioned above.

This paper is split into four different sections. First, cutting mechanisms in the machining of brittle materials are presented. Then, three simulation methods as well as existing research in these topics for the machining of ceramics are presented: FEA (Finite Element Analysis), SPH (Smoothed Particle Hydrodynamics) and DEM (Discrete Element Method), as well as the coupling of FEA and SPH. Following a short comparison between these simulation methods, simulation methods for the machining simulation of composite materials at microscale are presented. Here, the geometrical modelling of Ceramic Matrix Composites at microscale and a FEA material model for the simulation of composites are presented. For each material model, a short introduction

* Corresponding author.
E-mail address: simon.unseld@hs-augsburg.de (S. Unseld).

https://doi.org/10.1016/j.oceram.2023.100454
Received 7 July 2023; Received in revised form 30 August 2023; Accepted 2 September 2023
Available online 9 September 2023

to the theoretical fundamentals as well as an application to the machining process will be given, where different papers regarding the specific topic will be discussed.

To combine the different aspects to machining simulation of CMC and therefore give an outlook on future development, an orthogonal cutting simulation of chemical vapor infiltrated silicon carbide fiber reinforced silicon carbide (CVI SiC/SiC) at microscale is performed and compared with experiments.

2. Cutting mechanisms in brittle materials

Orthogonal cutting method for machining materials with a geometrically defined cutting edge, in which the tool is always aligned perpendicularly to the cutting direction. The cutting edge of the tool is wider than the part's surface. Since the cutting geometry is identical over the entire component width, the process may be reduced to a two-dimensional approach (Atkins 2009).

Furthermore, no tool rotation occurs in this method as compared to other machining processes (grinding, turning, milling, sawing), which further simplifies the somewhat complex modelling of the tool's kinematics and allows for a reduced number of process parameters to be utilized. Tool parameters in this process include the cutting depth ap, the feed rate vf, the clearance angle α, the wedge angle β, and the rake angle γ. Fig. 1 a) illustrates the general machining process in three dimensions, Fig. 1 b) shows the simplified in-plane model, as well as the different process parameters for this method [17].

For angular relationships of the tool, the following formula with respect to the normal of the machining direction (Fig. 1, right, black line) reads as follows:

$$\alpha_0 + \beta_0 + \gamma_0 = 90^\circ \tag{1}$$

whereas.

α_0: Clearance Angle
β_0: Wedge Angle
γ_0: Rake Angle

Compared to ductile materials such as metals, brittle materials form cracks during processing, which are propagated by different types of crack openings. These load cases can be described within the context of fracture mechanics by the elementary crack opening types, also called modes. Here, a distinction between the symmetrical lifting of the crack edges (tensile loading, mode I), the sliding of the crack edges in the direction of the crack (in-plane shear, mode II) and the sliding of the crack edges transverse to the direction of the crack (out-of-plane shear, mode III) is made. The directions of the crack opening modes in this case are defined for the local crack. A description of the modes is shown in Fig. 2.

While metallic materials such as titanium, aluminum or steel form a relatively long, spiral-shaped chip, the material removal in brittle-hard materials results via break-outs. When entering the material, a crack is formed in front of the cutting edge (cf. Fig. 3 a)), which progressively propagates and fractures at the primary deformation zone when the maximum load capacity is exceeded. This crack propagation is described by two superimposed effects: a Mode I tensile load, which steadily widens the crack, and a Mode II shear load, which causes the chip to shear off the surface (cf. Fig. 3, b)).

By simplifying geometry and kinematics and reducing the number of process parameters, orthogonal cutting is suitable for analyzing the general failure mechanics of a material in both real and numerical environments. Numerical analyses of the material behavior during machining include applications for brittle materials such as lime glass, unsintered alumina and silicon carbide, which will be discussed in more detail in Chapter 3.

This type of analysis is also important for composites such as CFRP (carbon fiber reinforced plastics) and CMCs (Ceramic Matrix Composite) to gain a better insight into the machining process. For brittle-hard materials such as CMCs, similar phenomena can be observed in machining as for purely monolithic brittle materials. However, due to the fibers embedded in the material, an anisotropic behavior of the material is present and affects the machining process as well.

According to Ref. [20], three possible scenarios can occur if the blade enters parallel to the fiber direction, depending on the maximum shear stress that arises. In the first scenario, the shear force of the tool exceeds the maximum shear stress tolerance of the entire composite, causing discontinuous chips to form (cf. Fig. 4, a)). If the shear force induced by the tool is below the maximum shear capacity of the whole composite but exceeds the maximum shear capacity of the matrix, the fibers compress and bend, while the matrix shears. This results in brittle removal of the material as the initial crack propagates along the fiber-matrix interface. For ceramic matrix composites, the fiber-matrix interface is the weakest point of the composite, which means that the crack can propagate the easiest in this area (cf. Fig. 4, c)).

If the fibers are perpendicular to the machining direction, similar scenarios can be derived from the previous case. A distinction is made between particularly high shear loads on the blade with the formation of discontinuous chips and shear loads under the shear load resistance of the matrix, resulting in crack growth in front of the blade. In the case of across fibers, the resulting crack can propagate particularly far (cf.

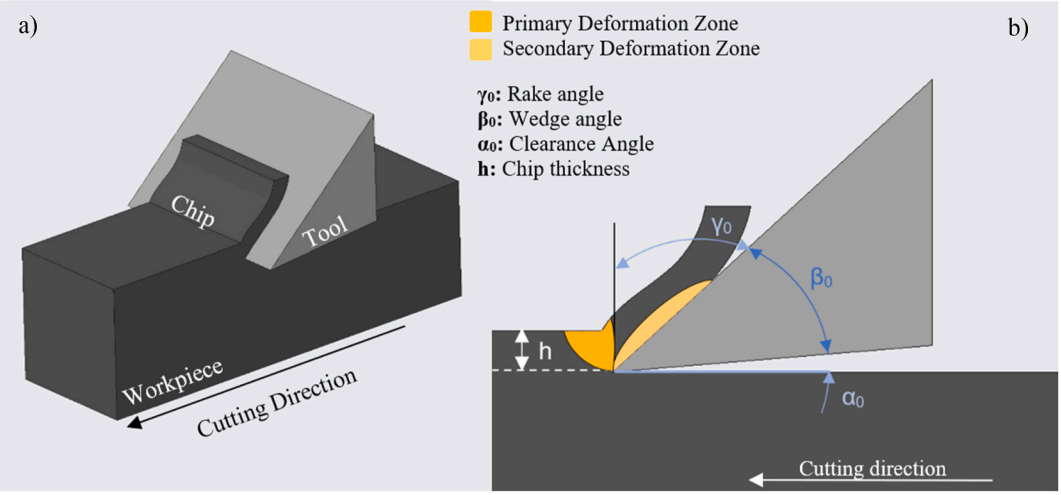

Fig. 1. 3D Orthogonal Cutting a), corresponding geometric parameters b).

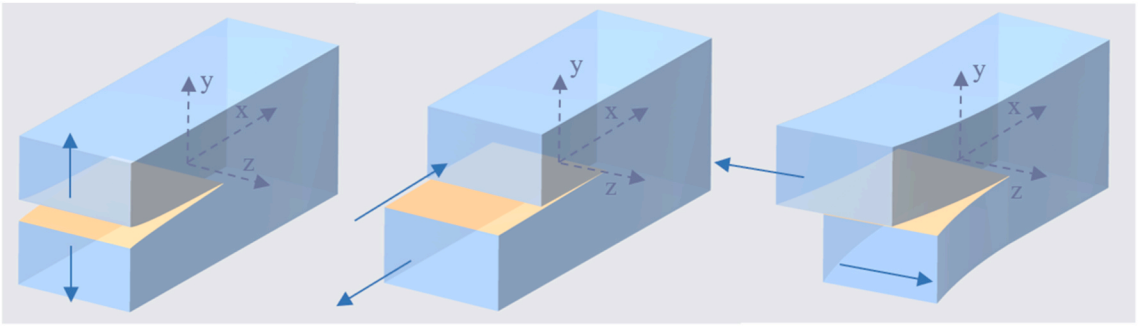

Fig. 2. Types of crack initiation: Mode I, tensile loading (left), Mode II, in-plane shear (centre), Mode III, out-of-plane shear (right).

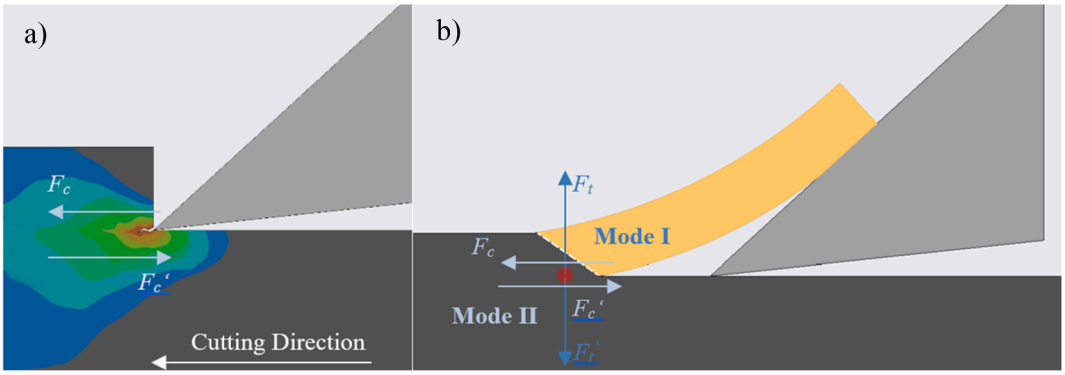

Fig. 3. Crack initiation by stress concentration a), crack propagation b) [18,19].

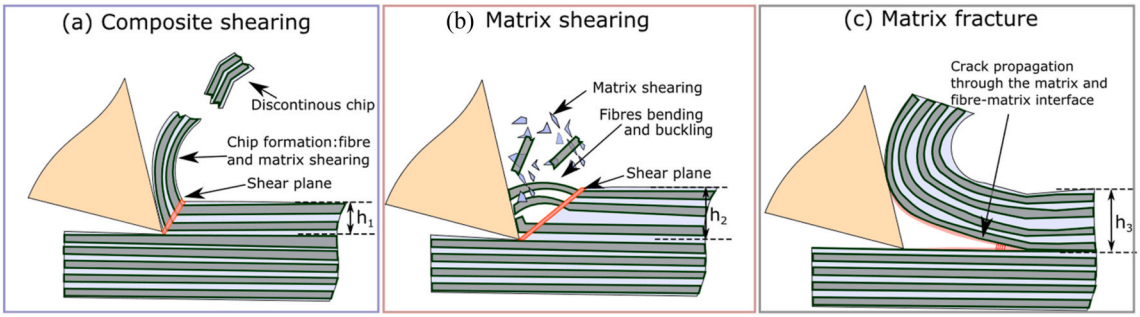

Fig. 4. Ablation mechanisms for ceramic matrix composites with fibers parallel to the machining direction: a) shear failure of the composite, b) shear failure of the matrix, c) crack propagation via fiber-matrix interface [20].

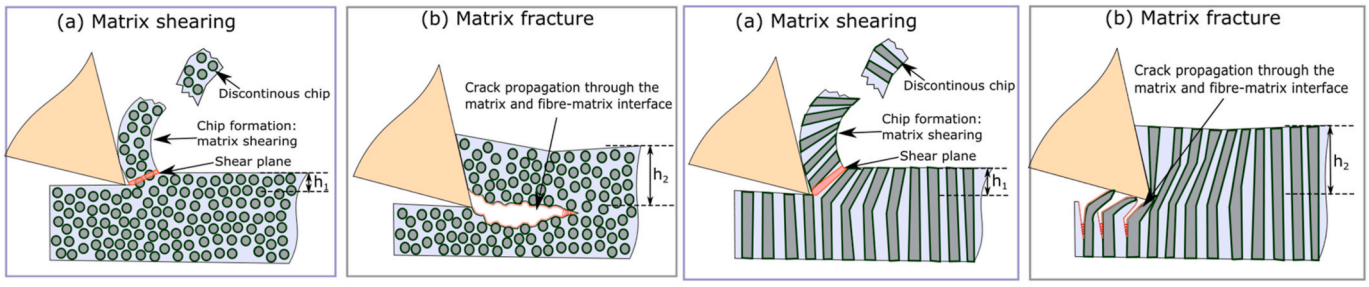

Fig. 5. Removal mechanisms for ceramic matrix composites with fibers perpendicular to the machining direction: a) Shear failure of the matrix, b) Crack propagation via fiber-matrix interface [20].

Fig. 5, left, whereas in the case of transverse fibers, crack formation takes place in depth, as the fibers prevent crack propagation in the cutting direction (cf. Fig. 5, right).

These considerations are reduced to a micro-scale perspective, in which the fiber direction of a fabric can be simplified to a great extent. Nevertheless, these theoretical basics offer insight into the phenomena present in the machining of brittle composites. Based on the previous fundamentals, the numerical description of different models for the

machining simulation of brittle monolithic materials will be presented in more detail in the following chapter.

3. Simulation methods for the machining of ceramics

In contrast to structural simulations, which take place within the elastic region of materials, machining simulations involve large deformations that can cause geometries to separate, crack or fracture. To address these challenges, different methods can be applied. To describe a continuum, mesh discretization is used to create a mesh of different elements that are connected to each other via nodes (Fig. 6, center). Thereby, the distortion of the elements poses a challenge in the description of large deformations. In contrast to a continuous mesh, particle discretization utilizes particles that can move relative to each other by using different bonding methods. (Fig. 6, right).

In this chapter, the different methods of discretization and their theoretical approaches to numerical simulation are discussed. The next subchapter introduces the dynamic finite element method (mesh discretization) of Johnson and Holmquist, which was developed for the simulation of dynamic problems involving brittle-hard materials such as ceramics or rocks. Furthermore, the theoretical methods of discrete elements (particle discretization) and smoothed particle hydrodynamics (particle discretization) are presented in more detail.

3.1. Finite element method

3.1.1. Theoretical fundamentals

Originally developed for impact simulation of ceramic materials, the constitutive model of [21] is used to describe failure behavior of brittle materials. The improved version of the model originally published in 1992 is known as the Johnson Holmquist 2 model (hereinafter referred to as JH-2 model).

Damage in ceramic materials begins by the development of small cracks that can progress to larger fractures. The model therefore has three stages to describe different material states: intact, damaged, and fractured. To define damage as such, the JH-2 model introduces the state variable D, which evolves as the component deforms and can be derived from the local pressure. This variable can take on values between 0 and 1, where 1 describes a completely damaged and 0 a completely undamaged material. It also considers elasto-plastic deformation and damage evolution.

The material model thus features a pressure-dependent strength, which is transferred to the three load stages of the material (intact, damaged, fractured). The individual load stages have their own functional equations, reflecting the stresses for this stage in representative form. These stresses are functions of the normalised equivalent stress, which is determined from the ratio of the actual local stress to the equivalent stress at the Hugonoit elasticity limit (HEL). HEL refers to a transition point in the material-specific properties of shock loads from linear-elastic to elastoplastic behavior and serves as an important indicator for the analysis of ceramics. The hydrostatic pressure occurring in this process is referred to as P_{HEL} and the corresponding stress as σ_{HEL}, with P_{HEL} taking values between 0.2 and 20 GPa for ceramics. If the resulting pressure of a shock load exceeds the HEL, the shear strength of the material is greatly reduced, and the material begins to behave like a fluid.

The normalised equivalent stress with respect to HEL is calculated as follows:

$$\sigma^* = \sigma_i^* - D\left(\sigma_i^* - \sigma_f^*\right) = \frac{\sigma}{\sigma_{HEL}} \tag{2}$$

whereas.

σ*:Normalised equivalent stress
σ_i*: Equivalent stress for intact material
σ_f*: Equivalent stress for fractured material
σ: Local stress

The equation of state for the intact material without damage (D = 0) is described by means of the material constants A, C, N and T to be as follows:

$$\sigma_i^* = A(P^* + T^*)^N(1 + C \bullet \ln \dot{\varepsilon}^*) \tag{3}$$

whereas.

P*: Normalised pressure (P/P_{HEL})
P: Hydrostatic pressure
$\dot{\varepsilon}^*$**: Equivalent Strain** ($\dot{\varepsilon}/\dot{\varepsilon}_0$)
$\dot{\varepsilon}_0$**: Material** constant = $1.0s^{-1}$
A: Material parameter
T: Maximum hydrostatic pressure under tensile load
T*: Normalised maximum hydrostatic pressure under tensile load (T/P_{HEL})
N: Material parameter
C: Material parameter

If damage occurs (0<D < 1), the following equation of state applies:

$$\sigma^* = \sigma_i^* - D\left(\sigma_i^* - \sigma_f^*\right) \tag{4}$$

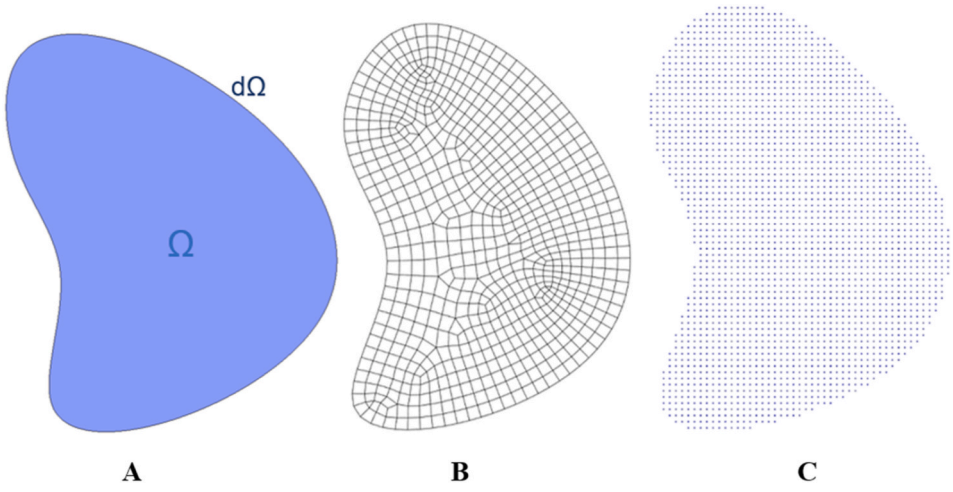

Fig. 6. Characterization of surfaces: Continuum body (A), body discretized by meshing (B) as well as body discretized with particles (C).

whereas.

σ*: Normalised stress (σ/σ_{HEL})
σ_f* Equivalent stress of the fractured material
σ_i*: Equivalent stress for the intact material

In the case of fracture (D = 1), the following relationship applies, considering the material constants B, C and M:

$$\sigma_f{}^* = B(P^*)^M(1 + C \bullet \ln \dot{\varepsilon}^*) \tag{5}$$

whereas.

σ_f*: Equivalent stress of the fractured material
$\dot{\varepsilon}^*$**:** Normalised strain ($\varepsilon/\varepsilon_{HEL}$)
B: Material parameter
M: Material parameter
C: Material parameter

Fig. 7 shows the relationship between normalised equivalent stress Sigma and normalised pressure P as a function of damage for the JH2 model.

The normalised pressure P can be coupled with the volumetric strain μ via the following relationship:

$$\begin{cases} P = k_1\mu + k_2\mu^2 + k_3\mu^3 + \Delta P_{n-1} & Compression \\ P = k_1\mu & Tension \end{cases} \tag{6}$$

whereas.

P: Hydrostatic pressure
μ: Volumetric strain
$K_{1,2,3}$: Material specific constants
ρ:Current density [m^3/kg]
ρ_0: Initial density [m^3/kg]
ΔP_{n-1}: Bulking Pressure [Pa]

Volumetric strain is calculated as:

$$\mu = \frac{V}{V_0} - 1 = \frac{\rho}{\rho_0} - 1 \tag{7}$$

whereas.

V: Current volume [m^3]
V_0: Initial volume [m^3]
K1 is a constant that describes the compression modulus. Based on the equation of state, the damage variable is defined by:

$$D = \sum \frac{\Delta\varepsilon^P}{\varepsilon_f{}^P} = \sum \frac{\Delta\varepsilon^P}{D_1(P^* + T^*)^{D_2}} \tag{8}$$

whereas.

$\Delta\varepsilon^P$: Plastic Strain during a cycle of integration
ε_f^P: Plastic strain to fracture under constant pressure
$D_{1,2}$: Damage constants
The plastic strain to fracture ε_f^P can be defined as follows:

$$\varepsilon_f{}^P = D_1(P^* + T^*)^n \tag{9}$$

The relationship between equivalent plastic fracture strain and normalised pressure is visualized in Fig. 8, left. The relationship between volume and pressure can be seen in Fig. 8, right.

3.1.2. Application to machining processes

[23] investigated the influence of ultrasonic-assisted polishing of SiC using the JH2 material model. The validation of the simulated results was supported by theoretical principles for the calculation of subsurface damage as well as by a test series. The results between simulation, theory and experiment are in good agreement with each other. Fig. 9 shows a part of the investigated influences of the work of Gu et al. using the example of vertical vibration amplitude.

Zhu et al. simulated the influence of speed and depth of cut on surface quality with a numerical simulation using the JH2 model for SiC. The scratch tests were carried out in the 2D domain and compared with the theoretical maximum chip height. Fig. 10 shows a comparison for the cutting depths 0.3 μm and 2 μm.

Table 1 shows a summary of publications dealing with the machining simulation of ceramics using FE models.

3.2. Discrete element method

The Discrete Element Method (DEM) is a numerical approach first postulated by Ref. [27] for the description of granular assemblies. The model later allowed the description of the fracture mechanics of brittle materials such as rocks [28,29], concrete [30], as well as multi-layer glasses [31,32] and ceramics [33–37].

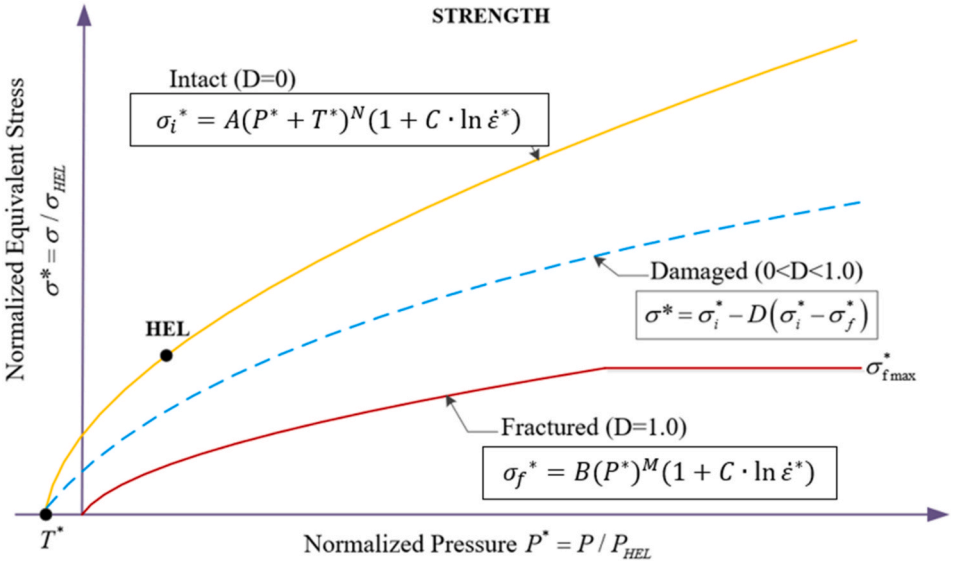

Fig. 7. Strength model of the JH-2 constitutive model [22].

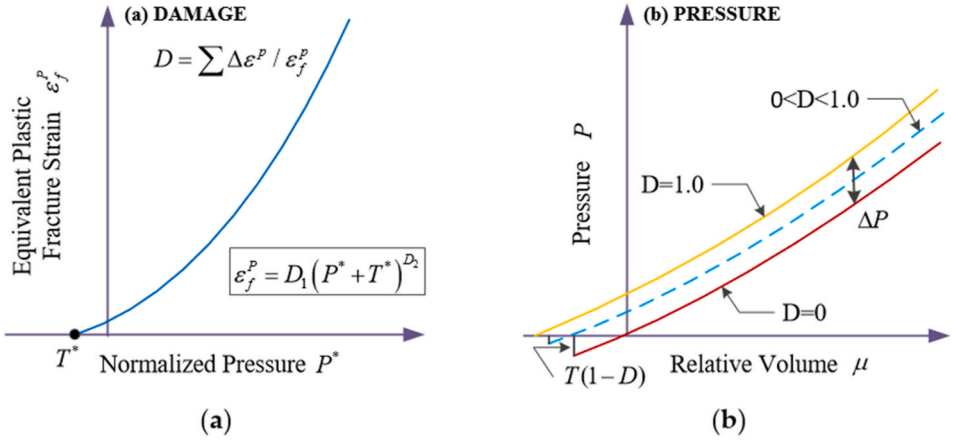

Fig. 8. Damage model (a) and EOS model (b) of the JH-2 constitutive model [22].

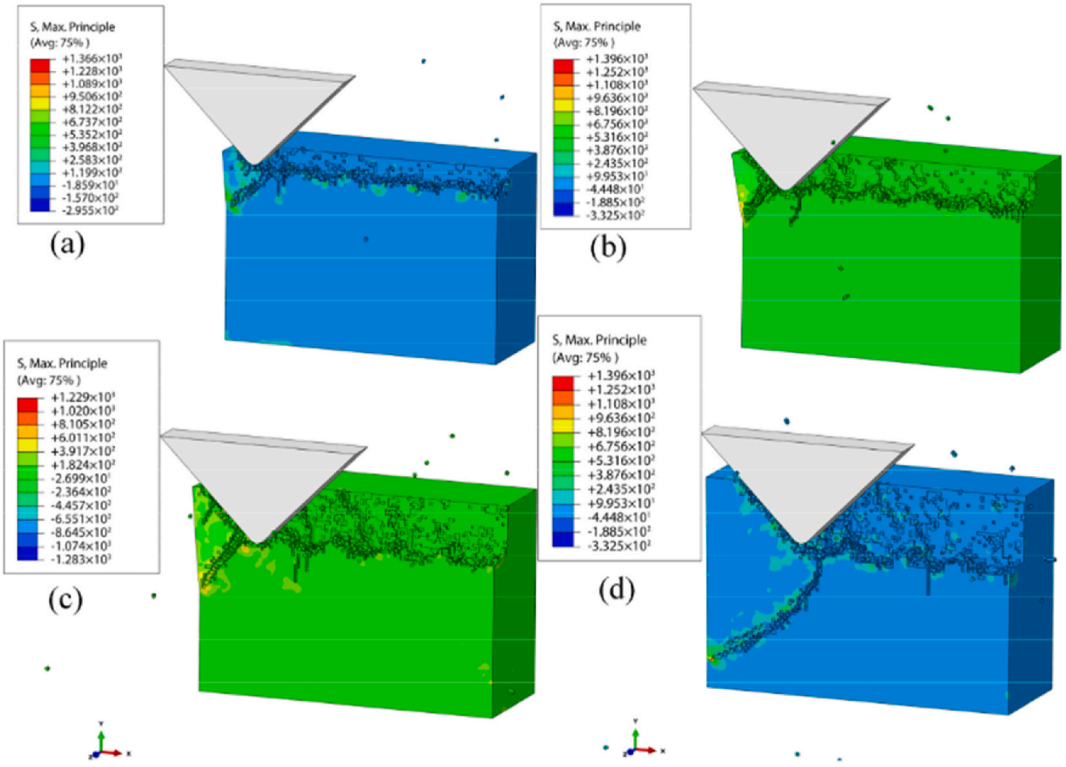

Fig. 9. Effect of vertical amplitude on subsurface damage with a vertical amplitude of: (a) 1 μm; (b) 2 μm; (c) 3 μm; (d) 4 μm [23].

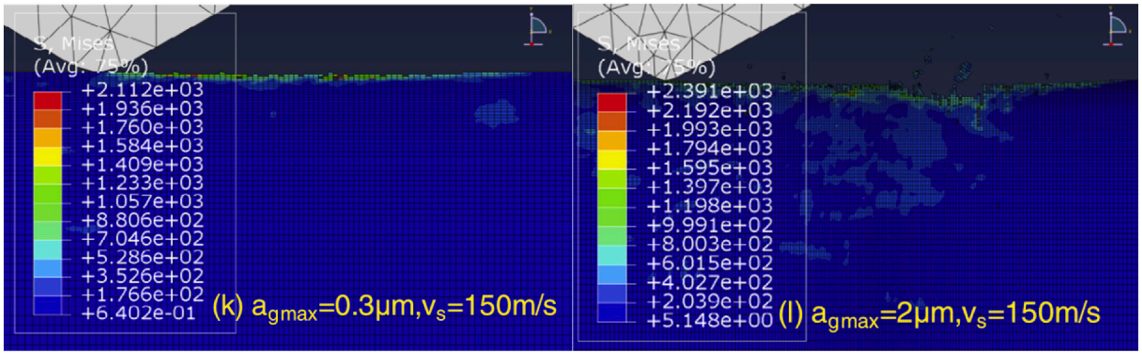

Fig. 10. Surface removal at different cutting depths: 0.3 μm (left), 2 μm (right).

Table 1
Application examples for machining brittle-hard materials using FE models.

Source	Material	Machining Process	Validation
[24]	SiC_p/Al	Orthogonal (2D)	–
[25]	SiC	Polishing (3D, Single-Grain)	–
[26]	SiC	Scratch test (2D)	M-UCT (Maximum Undeformed Chip Thickness), Theory to test series
[23]	SiC	Vibration Assisted Polishing	Theoretical calculation of the subsurface damage and comparison to scratch test series using white-light interferometry

As opposed to the continuum approach of the FEA, the DEM models the geometry via typically spherical bodies within a target volume. The overall object is analysed by examining the movement of individual particles, the contact surfaces of which are coupled with each other by bonding forces. The formation of micro- or macrocracks (cf. Fig. 11, left), which are typical for ceramic materials, can thus be described in this model by local exceeding of binding forces between two or more spheres (cf. Fig. 11, right) [33].

3.2.1. Theoretical fundamentals

Newton's second axiom and the displacement law are used to describe the contact between two particles [27]. Through the contact of two elements, the acceleration of the particle can be derived with the help of Newton's second axiom. By implementing the displacement law, the resulting contact forces of the touching elements are updated. Newton's equation of motion can be stated as follows:

$$\textit{Translation}\quad m_{(x)}\ddot{x}_i = \sum F_{(x)i}$$

$$\textit{Rotation}\quad I_{(x)}\ddot{\theta}_{(x)} = \sum M_{(x)}$$

whereas.

$m_{(x)}$: Mass of the particle [kg]
x_i: Acceleration of the particle [m/s^2]
$F_{(x)i}$: Acting forces [N]
$I_{(x)}$: Moment of inertia of the particle [N/m^4]
$\ddot{\theta}_{(x)}$: Angular acceleration of the Particle [rad/s^2]

The description of the contact between two particles can be achieved with the use of a spring-damper system with the inclusion of frictional properties (cf. Fig. 12).

The spring component by normal force of the system can be described in the following form:

$$\Delta F_n = k_n(\Delta n) = k_n((\dot{x}_i - \dot{y}_i)e_i)\Delta t \tag{10}$$

whereas.

Δn: Relative displacement of the particles [m]
k_n: Normal stiffness [N/m]
$\dot{x}_i, \dot{y}_i$: Resulting velocity [m/s]
Δt: Time interval (t_1-t_0) [s]

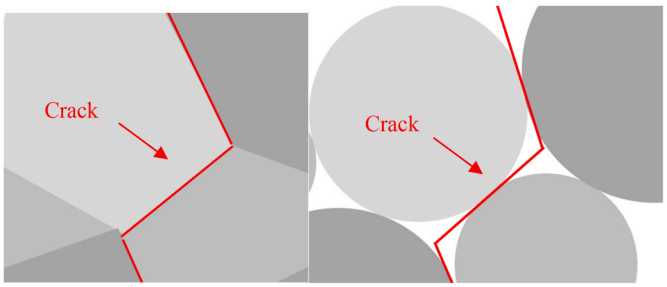

Fig. 11. Crack propagation of a microstructure in ceramics (left), equivalent crack propagation using discrete elements (right).

where for e_i:

$$e_i = \frac{y_i - x_i}{D} \tag{11}$$

whereas.

x_i: Particle centre X-coordinate [m]
y_i: Particle centre Y-coordinate [m]
D: Distance between center of two particles [m]

The spring portion of the system in the thrust direction is defined as follows:

$$\Delta F_s = k_s \Delta s = k_s\left((\dot{x}_i - \dot{y}_i)t_i - \left(\dot{\theta}_{(x)}R_{(x)} + \dot{\theta}_{(y)}R_{(y)}\right)\right)\Delta t \tag{12}$$

The summation of the shear and normal force components can be coupled via the following relationship:

$$(F_n) = (F_n)_{N-1} + \Delta F_N \quad (F_s) = (F_s)_{N-1} + \Delta F_s \tag{13}$$

The friction is considered by the friction law according to Coulomb:

$$(F_s) = F_n \tan \varphi_u + c \tag{14}$$

whereas.

φ:Friction angle
c:cohesion

3.2.2. Calibration process

The parameters used in the DEM describe the behavior of particles on a microscopic level. To apply macroscopic parameters such as Young's modulus or Poisson's ratio to this model as well as correctly represent phenomena such as crack development, the parameters of the DEM must be calibrated. This calibration can be done by analytical derivation, trial-and-error processes or via optimization loops.

An analytical derivation is possible if a uniform arrangement of the particles in space is present. According to the laws of energy conservation, the microscopic parameters can be derived from the macroscopic values in 3D space according to Ref. [38] as follows:

$$k_n = \frac{-\sqrt{2}ER}{2(1-\nu)} \quad k_s = \frac{1-3\nu}{1+\nu} \tag{15}$$

whereas.

k_n: Normal Stiffness

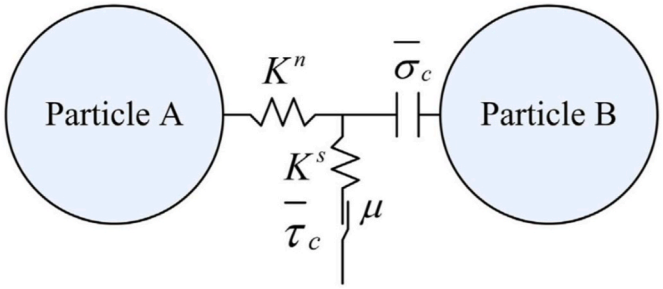

Fig. 12. Ball to ball contact model for the discrete element method [33].

k_s: Tangential Stiffness
R:Particle Radius
E: Young's-Modulus
v: Poisson's Ratio

The simpler case for the observation in-plane (2D) results according to Refs. [39,40] as:

$$k_n = \frac{-\sqrt{3}ER}{3(1-\mathrm{v})}$$

$$k_s = \frac{1-3\mathrm{v}}{1+\mathrm{v}}k_n \tag{16}$$

As an alternative to theoretical approaches, the material behavior can be described via optimization loops and trial-and-error processes (see Fig. 14). Numerical tests such as 3-point bending tests, compression tests, Brazilian tests and others can be used to approximate the micro-parameters of the model in relation to the macro-values from actual test series [34]. used the example of alumina in the green state to show the numerical approximation of the characteristic values for 3-point bending (cf. Fig. 13, left) and compression tests (cf., Fig. 13, right).

The basic procedure for calibrating the micro parameters of the DEM is shown in Fig. 14.

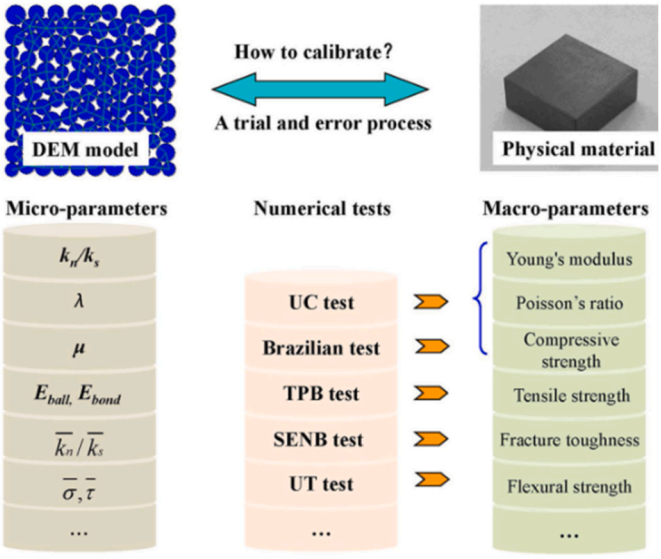

Fig. 14. Calibration process for the discrete element method according to [41].

3.2.3. *Application to machining processes*

[29] addressed the numerical investigation of the machining process of sandstone using the discrete element method. Numerical uniaxial tension and compression tests were carried out to calibrate the numerical model. In the numerical test series, it could be shown that a transition from ductile to brittle removal behavior occurs with an increase in the depth of cut. The validation of the simulated data is carried out via the experimental and numerical determination of the ratio of the specific energy ε to the compressive strength σ_c, which are in good agreement with one-another. Furthermore, images (cf. Fig. 15) were taken using a high-speed camera to compare the removal mechanism. These also correspond well to the real behavior.

[34] investigated the machining of unsintered alumina for different cutting speeds and depths of cut. The calibration of the DEM model was hereby carried out via compression tests and 3-point bending tests. The validation of the model was carried out by comparing the machining forces between the numerical and the real model, and high-speed recordings of the machining process were used as well (cf. Fig. 16). The deviation from reality thereby amounts to between 1 and 7% depending on the cutting speed.

[37] investigated the machining process of soda-lime glass via a

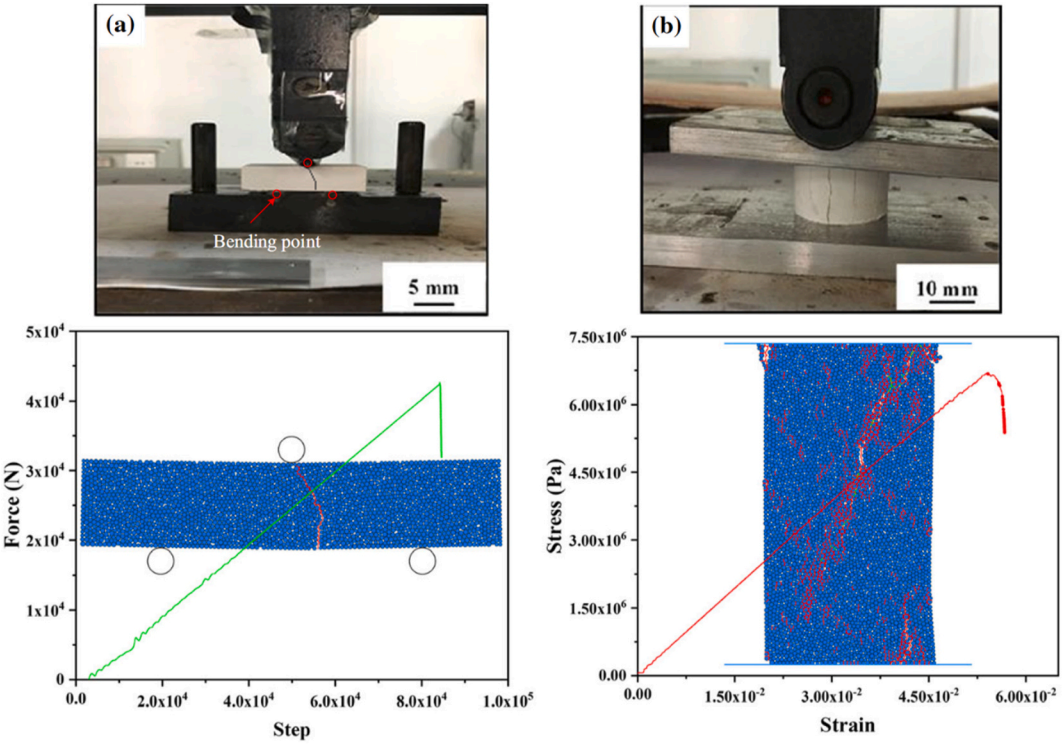

Fig. 13. Calibration tests for DEM microparameters: 3-point bending test and associated DEM simulation (a) as well as compression test with associated DEM simulation (b) for green aluminum oxide [34]. (For interpretation of the references to colour in this figure legend, the reader is referred to the Web version of this article.)

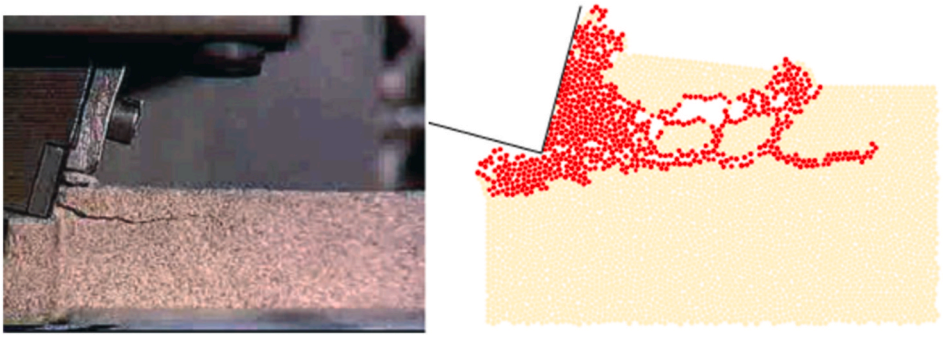

Fig. 15. Machining of rock at a cutting depth of $a_p = 4$ mm (left), DEM simulation with a cutting depth-to-particle radius ratio $a_p/R = 25$ [29].

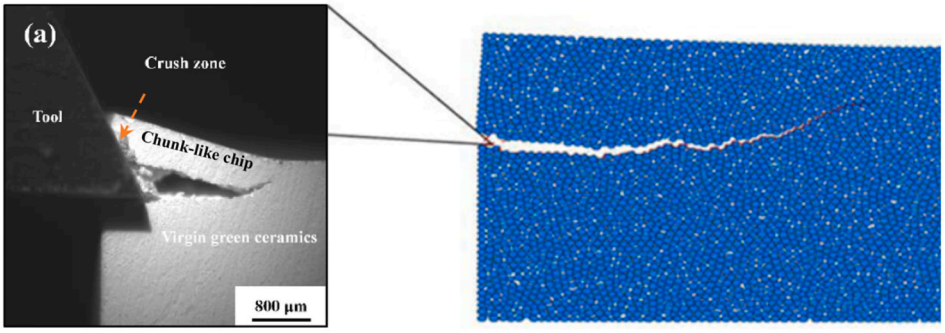

Fig. 16. Orthogonal cutting of unsintered aluminum oxide: Machining test (left), simulation using DEM (right) [34].

comparable setup as in the previously presented work. The calibration of the micro-parameters was thereby carried out via uniaxial tensile and compression tests, whereby the modulus of elasticity, the tensile strength, the compressive strength and the Poisson's number were determined. The model was validated through comparison of the machining forces (profile and mean value) and through consideration of the surface integrity (cf. Fig. 17). In this case, the average machining force fluctuates at a maximum of 17%.

With a DEM model for the machining of CFRP with a fiber orientation of 0°, +45°/-45° and 90° [42], showed an approximate agreement of the real machining force with respect to the simulated data, whereby considerable fluctuations of the minimum and maximum machining force with a variation of up to 500 N are observable. Fig. 18 shows the simulation for the +45° and −45° fiber orientation, in which the discrete elements (spheres) are separated in acceptable agreement with reality.

Table 2 shows further literature in which the SPH method was used for the machining simulation of hard-brittle materials.

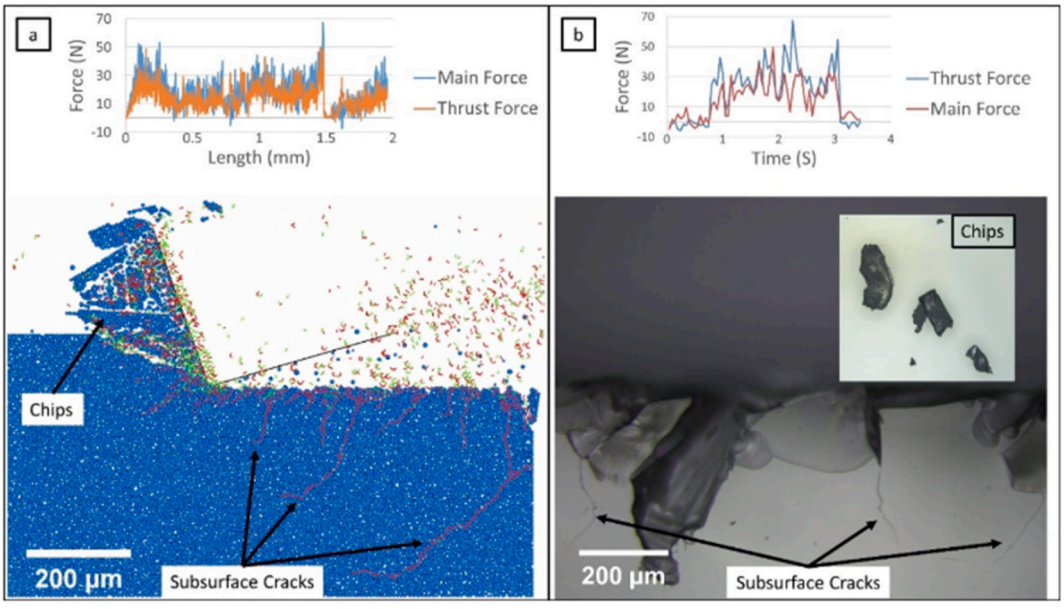

Fig. 17. DEM model of soda-lime glass (left) and machining test (right) with associated force curves [37].

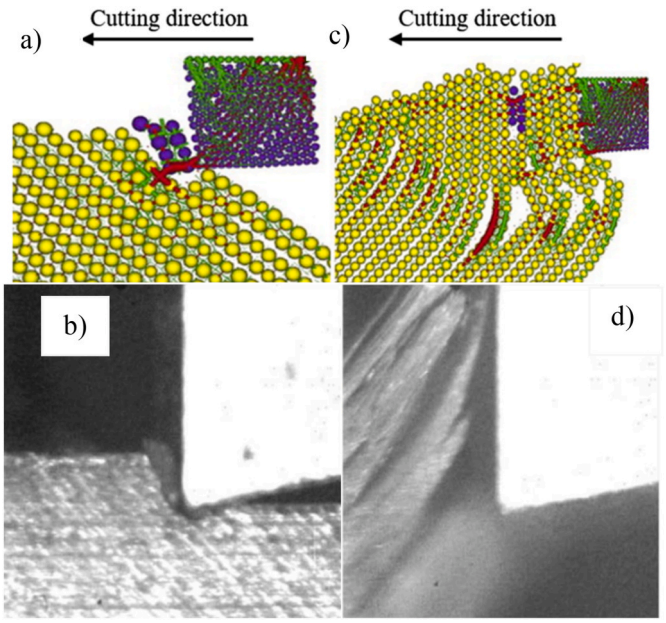

Fig. 18. DEM simulation of an orthogonal cutting: a) +45° fiber angle, b) associated high-speed image, c) fiber angle −45°, d) associated high-speed image [42].

3.3. Smoothed particle hydrodynamics

Smoothed Particle Hydrodynamics (SPH) is a method developed by Gingold, Monaghan and Lucy [44,45] in 1977 for the numerical description of astrophysical phenomena such as the collision of two planets. It is suitable for describing transient dynamic simulations of multiphase flows and flows on free surfaces [46,47], but also for impact simulations and machining simulations [48]. In this model, the volume under consideration is divided into discrete particles, with each particle having its own state variables such as mass and density. It is a mesh-free method capable of capturing large deformations of the original geometry [49]. The interaction between a particle and its environment is carried out within a defined area of influence. Using smoothing or kernel functions, weighted fractions can be considered depending on the distance of neighboring particles within the area of influence. The kernel function is a method of taking data as input and transforming it into the required form of data processing. As the distance of a neighboring particle to the target particle increases, its influence decreases towards the boundary of the influence area. Fig. 19 illustrates the influence of a particle (black) on its neighboring particles (blue) via the smoothing core W as a function of the distance Δx and the so-called smoothing length h.

3.3.1. Theoretical fundamentals

In the following, the theoretical principles of the calculation of the SPH model will be presented in more detail.

With the SPH method, the value of a variable with index i is calculated as a function of a set of neighboring particles (index j), which are located within the influence zone of the particle. Apart from mass and density, the influence of the neighboring particle also depends on the distance from the target particle, the smoothing length, and the smoothing function (see formula (17)).

$$\langle f_{(x_i)} \rangle = \sum_{j=1}^{N} \frac{m_j}{\rho_j} W_{(\Delta x, h_i)} f_{(x_j)} \tag{17}$$

whereas.

$\mathbf{W_{(r_{ab,h})}}$**:** Smoothing kernel function
Δx: Distance to neighboring particles [m]
$\mathbf{h_i}$**:**Smoothing length [m]
$\boldsymbol{\rho_j}$**:**Density of the particle in position x_j [kg/m^3]
$\mathbf{m_j}$**:**Mass of the particle in position x_j [kg]

Where the distance Δx is determined as follows:

$$\Delta x = |x_i - x_j| \tag{18}$$

whereas.

$\mathbf{x_i}$**:** Position of the particle i [m]
$\mathbf{x_j}$**:** Position of the particle j [m]

Especially in the field of machining simulation of brittle materials, a propagation of cracks and the associated separation of individual particles from one another is expected. Thus, it is necessary to vary the smoothing length accordingly. For example, when considering a separation process with a constant smoothing length, the distance between the particles scales accordingly until an unwanted influence by already separated particles occurs. Therefore, there are different approaches to vary the smoothing length accordingly. Here, the simplest method is to adapt the smoothing length using the so-called averaged density approach.

The SPH model is based on the laws of continuum mechanics, which makes it stable compared to empirical models. The Langrangian form of the continuum mechanics equations can be defined as follows:

$$\begin{aligned} \frac{d\rho}{dt} &= -\rho \nabla \bullet \underline{v} \\ \frac{dv}{dt} &= \frac{1}{\rho}\nabla\sigma + \frac{1}{\rho}\underline{b} \\ \frac{dr}{dt} &= \underline{v} \end{aligned} \tag{19}$$

Table 2
Application examples for machining brittle-hard materials with the DEM model.

Source	Material	Machining process	Validation
[34]	Al_2O_3 (unsintered)	Orthogonal cutting	Direct comparison of machining forces (simulation and test series), ΔF<1 N, max. deviation 7%.
[37]	Soda Lime Glass	Orthogonal cutting	Direct comparison of machining forces (simulation and test series), ΔF<2.5 N, max. deviation 17%.
(Jiang, Li, & Tan, 2015)	Polycrystalline SiC	Grinding (grinding wheel)	Indirect comparison of force tendencies for different parameters via test series, no reference values provided
[29]	Berea Sandstone	Orthogonal cutting	Specific energy/uniax. Compressibility ε/σ_c: 0.6–1.1 (simulation) to 0.6–0.7 (calculation)
[42]	CFRP	Orthogonal cutting	Comparison of force curves, deviations from min/max up to 500 N
[43]	Polycrystalline SiC	Scratch test (2D simulation)	Comparison of the surface: crack depth and from test (SEM) and simulation
[36]	95% Al_2O_3	Scratch test (3D simulation)	Comparison of surface: crack width, depth and shape from test (SEM) and simulation Comparison of machining forces from simulation and test (both below 2 N)

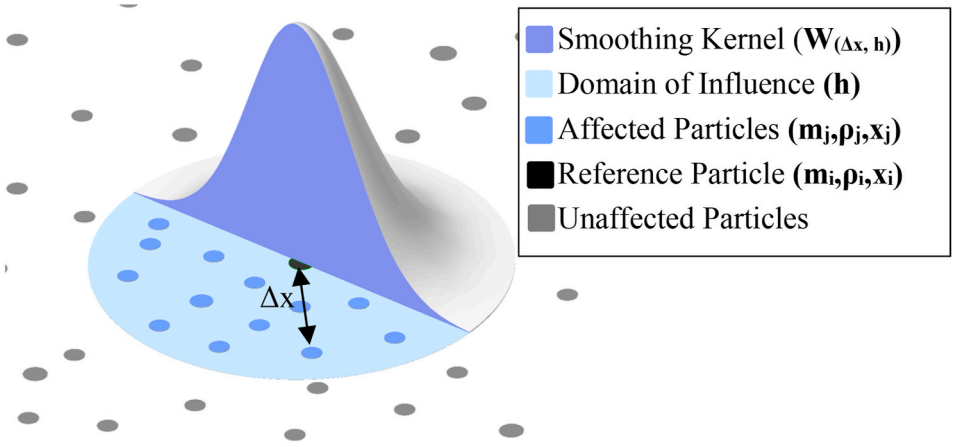

Fig. 19. Schematic diagram of smoothed particle hydrodynamics for a reference particle (black) with the smoothing core W (dark blue) in the influence area h (light blue). (For interpretation of the references to colour in this figure legend, the reader is referred to the Web version of this article.)

whereas.

ρ: Density
∇: Nabla operator
ν: Velocity vector
σ: Cauchy stress tensor
b: volumetric body forces
r: Position vector

Assuming a constant mass over all times t of all particles of the quantity j, the equations described in (20) can be approximated as follows:

$$\left\langle \frac{d\rho}{dt} \right\rangle_i \approx -\rho_i \sum_j \left(\underline{v}_j - \underline{v}_i \right) \bullet \nabla W_{ij} \frac{m_j}{\rho_j}$$
$$\left\langle \frac{dv}{dt} \right\rangle_i \approx \sum_j \left(\frac{\underline{\underline{\sigma}}_i}{\rho_i^2} - \frac{\underline{\underline{\sigma}}_j}{\rho_j^2} + \Pi_{ij} \underline{\underline{I}} + \underline{\underline{\Lambda}}_{ij} \right) \bullet \nabla W_{ij} m_j + \frac{1}{m_i} \underline{b}_i \tag{20}$$

whereas.

Wij: Kernel function ($W_h(\Delta x, h)$.
mi,j:Particle mass
vi,j:Particle velocity
Πij: Artificial Viscosity Term
$\underline{\underline{\Lambda}}_{ij}$: Artificial Viscosity Term
$\underline{\underline{\sigma}}_{i,j}$: Total Stress Tensor

The artificial viscosity terms account for numerical instabilities of the discontinuous process and therefore serve as stabilizers. The equation for calculating the conservation of energy is given by:

$$\left\langle \frac{d\varepsilon}{dt} \right\rangle_i = \frac{p_i}{\rho_i^2} \sum_j m_j v_{ij} \bullet \nabla_i W_{ij} + \frac{1}{2} \sum_j m_j \Pi_{ij} v_{ij} \bullet \nabla_i W_{ij} + \Gamma_i \tag{21}$$

whereas.

pi: Isotropic Pressure Component of the total Stress tensor
Γ_i: Rate of thermal energy per unit mass

The smoothing can be described using different approaches such as quadratic, cubic spline, B-spline, Gaussian, or higher order kernels. As an example, the cubic spline can be described as such:

$$W_{(\Delta x,h)} = a_D \begin{cases} 1 - \frac{3}{2}q^2 + \frac{3}{4}q^4 & \to 0 \le q \le 1 \\ \frac{3}{2}(2-q)^3 & \to 1 \le q \le 2 \\ 0 & \to q \ge 0 \end{cases} \tag{22}$$

3.3.2. *Application to machining processes*

Regarding the machining process, the SPH method proves to be particularly suitable for modelling crack propagation. Using the example of the scratch test of monocrystalline SiC with the Johnson-Holmquist-Cook material model [50], shows a high comparability between the numerical model and reality (cf. Fig. 20). Alongside the comparison of the force profiles of the numerical model and the test series, parameters such as the crack width and depth, but also optical comparisons of the removal mechanism are investigated in more detail as validation methods. Within the scope of this paper, different geometries are investigated, providing information on the influence of the scratch body geometry on the machining results. The validation shows a good correspondence of the numerical model with reality.

Using the SPH method with the Johnson-Holmquist model in a scratch test [51], showed the influence of different machining speeds on roughness, crack propagation and machining force for SiC. Thereby, different removal behaviors from ductile machining to the brittle-ductile transition zone and brittle removal were presented. (cf. Fig. 21). The numerical results were validated by comparing machining forces, surface roughness and the theoretical transition zone from ductile to brittle machining. The critical transition zone from ductile to brittle material removal was determined to be approx. 0.35 µm. With this numerically determined value close to the theoretical value of 0.3 µm, it can be concluded that the Johnson-Holmquist model is able to describe even the low ductile range of the material and is thus more accurate than the simplified brittle fracture model.

[52] addressed the machining simulation of zirconia using the SPH method. Based on the JH2 model, the influence of the tool rake angle on the machining quality was investigated. The validation thereby took place via the so-called M-UCT, maximum undeformed chip thickness. This characteristic value indicates the theoretical maximum removal depth at which ductile removal of the material is still possible. The results of the simulation show that a ductile removal below this theoretical limit is feasible and that the model therefore functions correctly within the investigated framework. Furthermore, the surface and chip formation from test series were used as methods for validation. With the variation of the tool geometry, different chip formations could be observed (cf. Fig. 22), which were also found in a similar form within the test series.

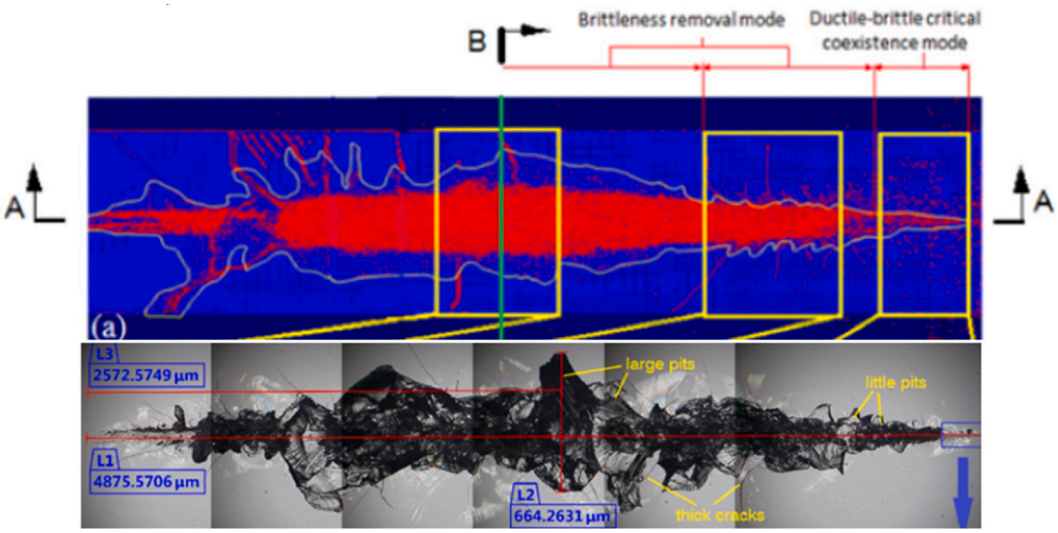

Fig. 20. Topography of a scratch test of monocrystalline SiC in simulation (above) and from tests (below) [50].

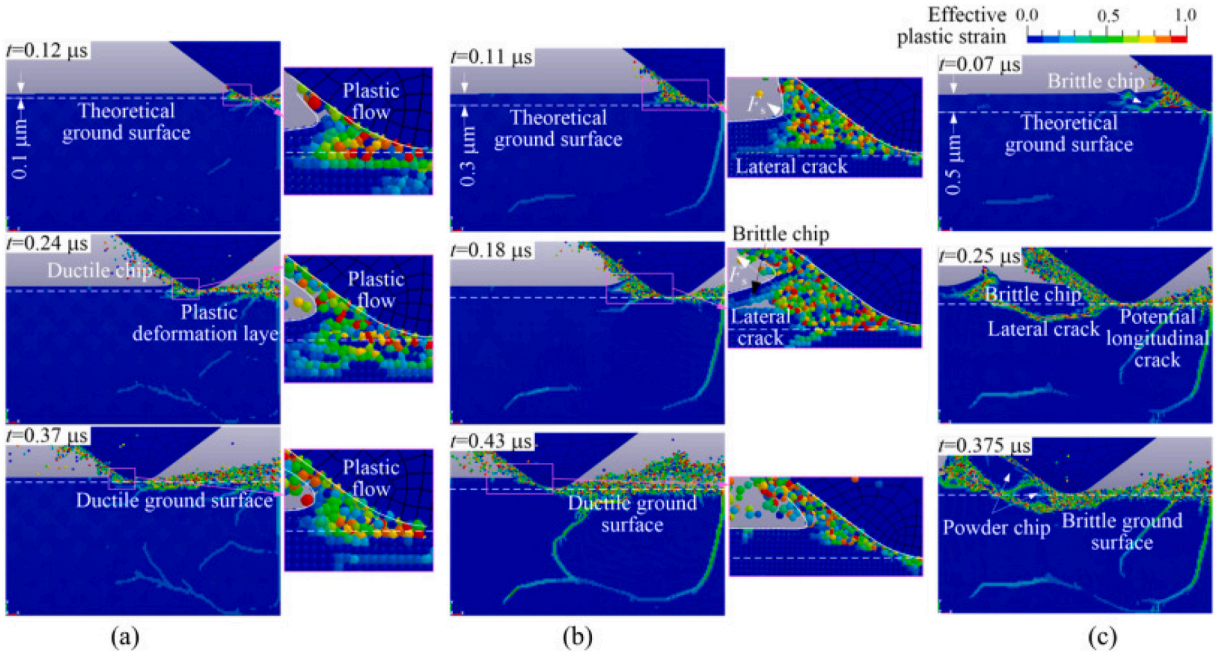

Fig. 21. Machining simulation of SiC for different cutting depths: a) 0.1 µm, b) 0.3 µm and c) 0.5 µm [51].

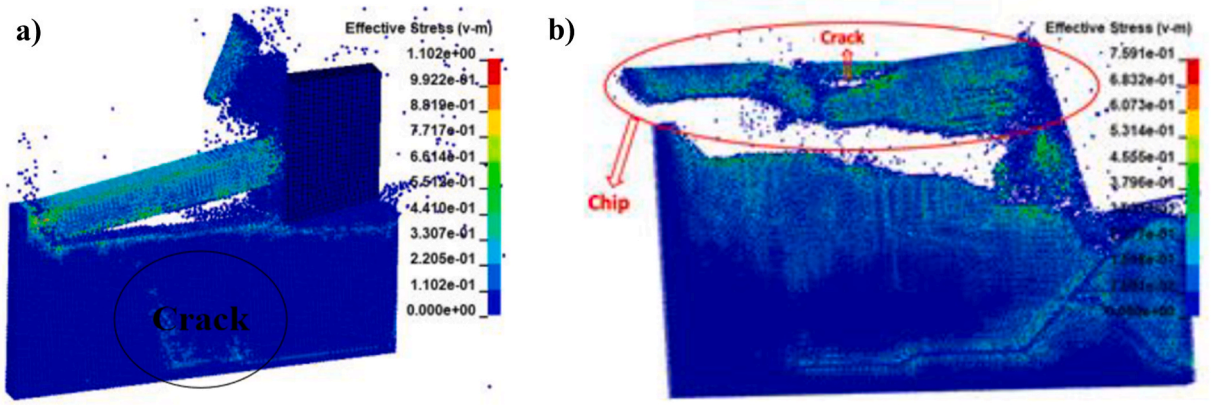

Fig. 22. Removal of zirconium oxide with a cutting depth of ap = 1 µm and 5 m/s: clearance angle = 0° a), clearance angle = −35° [52].

Table 3
Application examples for machining brittle-hard materials with the SPH model.

Source	Material (Material Model)	Machinig Process	Validation
[53]	Al 6061 (Johnson-Cook)	Orthogonal cutting/ turning	Comparison of chip formation and force (simulation and test series), ΔFmax<17%
[54]	Quartz glass (Johnson-Cook)	Orthogonal cutting	Surface, chip formation force curve ΔFmax<17%
[52]	Zircon (JH2)	Orthogonal cutting	Consideration of the theoretical BDT (Brittle to ductile Transition), chip formation
[51]	SiC (JH2)	Orthogonal cutting	Surface, machining forces and BDT (Brittle to ductile Transition)
[50]	Monocrystalline SiC (Johnson-Holmquist-Cook)	Single-Diamond-Grinding	Validation via machining force and surface roughness, very good agreement between force curve and damage patterns (test and simulation)
[55]	K9 Glass (JH2)	Orthogonal cutting	None

Table 3 shows further literature in which the SPH method was used for the machining simulation of hard-brittle materials.

3.4. Coupling FEA and SPH

Based on and developed according to the laws of continuum mechanics, the finite element analysis has the central disadvantage of complicated handling of discontinuous processes, such as those occurring in machining simulations.

As discussed in previous chapters, different, more appropriate methods such as DEM and SPH can be used to facilitate the handling of discontinuous processes. However, these methods have an increased computational cost at higher resolution, thus providing the benefits of improved discontinuity manageability at the expense of computational cost [56].

A combination of the computationally efficient FEA and discontinuity oriented SPH therefore offer a practical approach to improving simulations. Using the example of cutting the aluminum alloy A202-351 [53], demonstrated that the coupling of FE and SPH methods can reduce the calculation time significantly from 144 to 77 min, while maintaining the same quality (cf. Fig. 23).

For the most efficient and accurate simulation possible, the coupling of the FEM with the SPH method can thus be implemented to satisfy both the requirements for calculation quality and time. Finite elements can thereby be used at locations where the occurrence of a discontinuity is unlikely, while SPH particles can be used at locations with a high probability of crack propagation [56]. At the point of contact between the FEM and SPH elements, the area of influence of SPH particles is co-transferred to the nodes of the FEM (see Fig. 24). Since crack propagation can occur randomly to a certain extent, deviations can occur compared to reality in the simulation with the SPH method. A correct connection of FEM and SPH with the appropriate formulation may improve the accuracy of the simulation [57]. [58] showed that the coupling between FEM-SPH with the selection of an appropriate SPH formulation can have an error of less than 2% to reality, while other formulations can have up to 18% error.

Different methods can be used to couple the interfacing between SPH particles and FEA mesh. These methods include the tied-interface, the hybrid-element coupling and the nodes-to-surface method [56,59,60]. In the 'tied-Interface' method, SPH particles (slave) are created based on already existing nodes (master) of the FEA mesh to allow for a seamless interface between FEA and SPH (Fig. 25, left) [61]. The second method of hybrid element coupling introduces hybrid elements that serve as a transition layer between FEA nodes and SPH particles and thus a constraining bond between the two elements no longer applies (Fig. 25, middle). In the 'Nodes-to-Surface' method, a distinction is made between master and slave.

3.5. Comparison of the selected simulation methods

Customized for specific applications, the individual methods for numerical description provide a variety of different advantages and disadvantages, depending on the selected application. The differentiation of the methods for the respective application areas is thus a central factor in the simulation of the machining process of brittle monolithic as

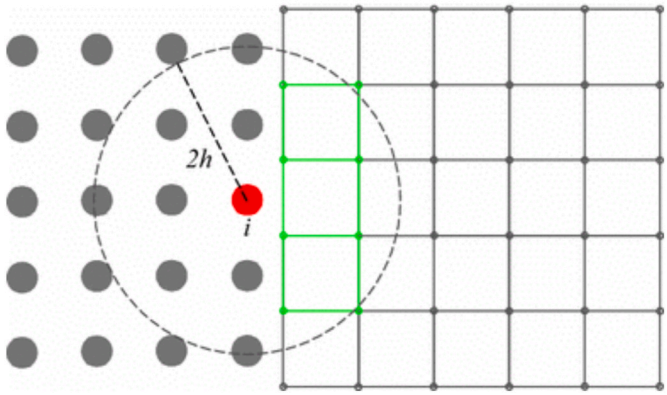

Fig. 24. Coupling SPH and FEM at the interface [59].

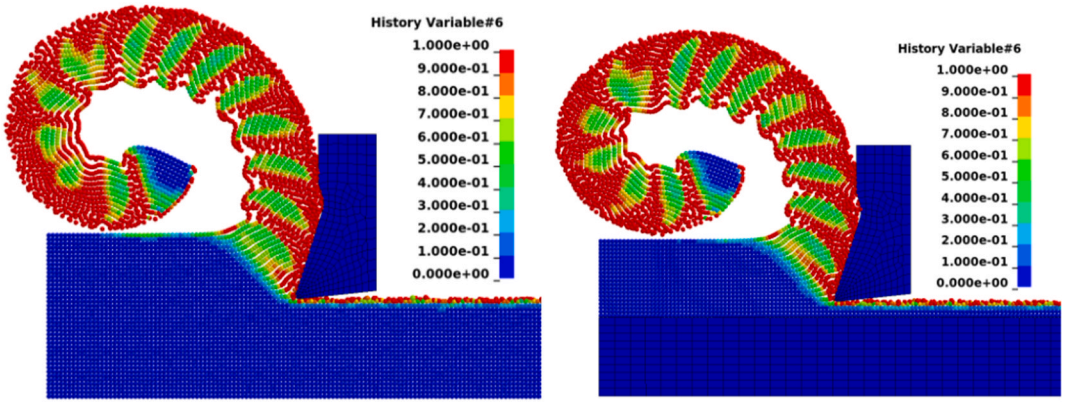

Fig. 23. Comparison of results with a pure SPH model (left) and a FE-SPH coupled model (right) for A202-351 [53].

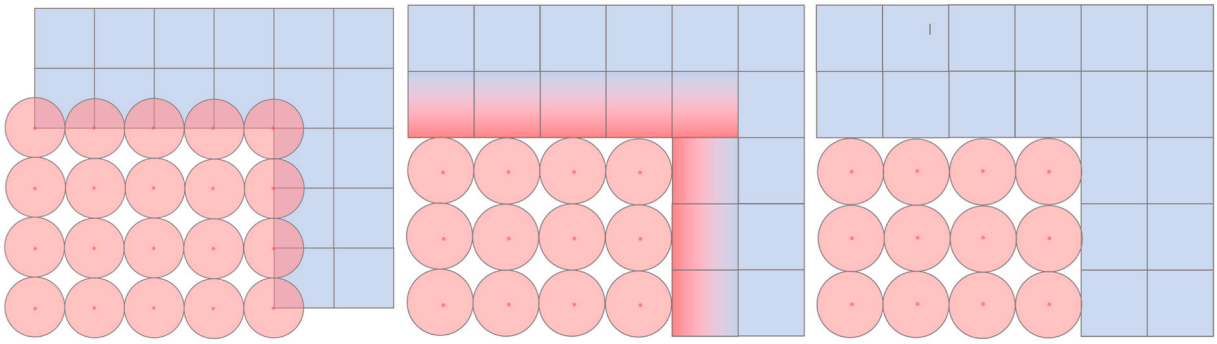

Fig. 25. Tied interface (left), hybrid element coupling (middle), ‚Nodes-to-surface' contact (right) [59].

well as composite materials. The objective of this chapter is thus to provide a deeper insight into the advantages and disadvantages of the individual methods. The methods presented in this framework are not the only methods that can be used in machining for the simulation of ceramics. Since the methods presented in this work are to be transferred to the field of CMC, methods are presented that provide the possibility of transferability to composite materials.

The discrete element method is a simplistic model in its formulation, capable of representing a large number of homogeneous and porous materials. Compared to the SPH, however, the formulation lacks consideration of dynamic effects that can arise from high impact velocities. For homogeneous, granular and brittle materials, DEM is very well suited, while SPH is suitable for more complex models where more sophisticated modelling approaches are required. The SPH method is much more flexible in its application due to the access to a large number of constitutive models from FEA, which are not possible to be represented via DEM. In order to limit the scope of this work, a limitation to the methods of FEA, SPH and DEM is necessary.

Compared to the DE and SPH methods, discontinuous processes are particularly difficult to describe within the FEA. Problems arise from instabilities such as extreme mesh distortions and the separation of individual nodes. Different methods for overcoming such problems, such as adaptive remeshing and the erosion of strongly distorted elements, allow the FEA to nevertheless describe highly non-linear problems. Especially for hard-brittle materials, where the propagation of fine cracks in the material is a central part of the erosion mechanism, particle discretization methods have a key advantage in describing these phenomena at the expense of additional computation time.

An overview of the advantages and disadvantages of the individual methods is listed in Table 4.

4. Simulation methods for the machining of composites at microscale

Compared to metals, the structural design of fiber composites differs depending on the observation of scale. Consequently, it is necessary to model the composite material in different scales, subdivided into micro, meso and macro scales (cf. Fig. 26). The macro scale describes the general geometry of the composite material in its entirety and covers a scale from a few millimetres up to several metres. The meso scale ranges from a few millimetres to several micrometres. In this range, the

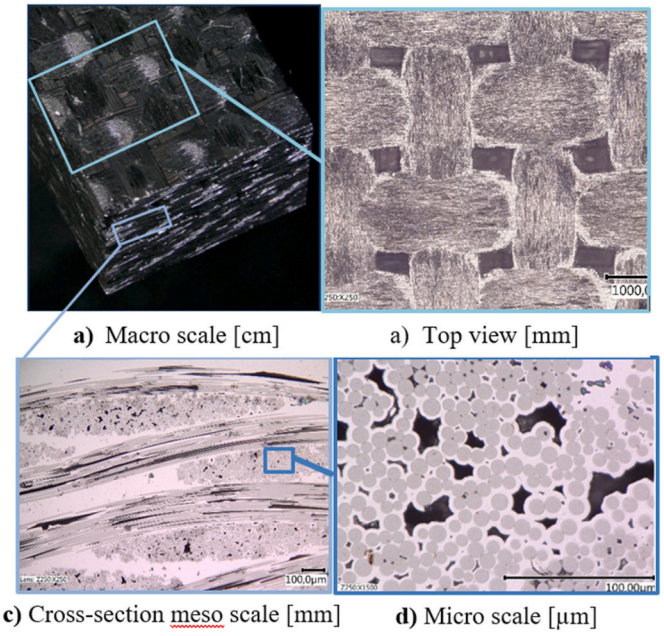

Fig. 26. Structure of a fiber composite material using the example of silicon carbide reinforced silicon carbide. (For interpretation of the references to colour in this figure legend, the reader is referred to the Web version of this article.)

structural composition of the fabric is examined in greater detail. The microscale ranges from several hundred micrometres down to a few micrometres. This range is particularly suitable for examining the composition of the microstructure or the structural composition within a fiber roving.

The division of the levels to be considered within the structural composition provides improved understanding of the origins and reasons for damage as well as removal mechanisms. In this chapter, subsequent to the models for brittle materials from chapter 3, the numerical modelling of brittle fiber composites will be dealt with in more detail. Besides the general geometric modelling, methods for describing the fiber-matrix interface will also be addressed.

Table 4
Advantages and disadvantages of selected methods for the simulation of machining processes.

Method	Advantages	Disadvantages
Finite element	Fast calculation, variety of constitutive models	Modelling for discontinuous processes demanding and inefficient
Discrete element	Representation of complex deformation processes, efficient calculation method for granular materials [62]	Simple model, complex calibration of micro-parameters [62]
Smoothed Particle Hydrodynamics	Representation of complex deformation processes, use of FE models	Time-consuming calculation, convergence, stability and accuracy depending on particle distribution [63]

4.1. Geometrical modelling

As described previously, a distinction is made in composites between the micro, meso and macro scale. The microscale describes a size range of several 100 μm, whereby individual fibers and their interaction with the matrix and its bonds are examined in more detail. In the mesoscale, which describes the size range of a few millimetres, the influence of the fabric is examined in more detail. Thereby, depending on the modelling, the interaction of individual fibers with the matrix is neglected and only the structure of the rovings is considered. The macroscale range considers the overall structure as an idealized body. Especially for machining processes, the consideration in the microscale range is of particular importance, since a multitude of damage types, which define the roughness of the surface in the macroscale, can be derived from the mesoscale and microscale. As a result, this chapter will focus on the modelling of the high-resolution microscale domain. A fiber composite material generally consists of 4 elements: The matrix, the fiber, the fiber coating, and the fiber-matrix interface (cf. Fig. 27).

The geometry is modeled by analyzing the microstructure (cf. Fig. 28). Depending on the material, the fiber diameter, the porosity, the matrix content and the size of the fiber-matrix interface are derived and virtually representative geometries are derived via statistical distributions of the individual components [67,68].

Images of the microstructure can be used via image-based analysis to study the composition in more detail. Using the example of extracting data from a SiC/SiC roving [67], reconstructed a 2D microscale geometry by evaluating the matrix, fiber and pore content. The key aspect for the strength of the composite material is the connection between the fiber and the matrix. In addition to the homogeneous material models, an additional coupling of the individual materials between each other must thus be performed. Here, the Cohesive Zone Model, or CZM for short, is used. This model will be presented in more detail in the following chapter.

4.2. Cohesive zone model

The Cohesive Zone Model (CZM) was first introduced by Refs. [69,70]. It can be used to describe the bonding strength between materials. Applications include the simulation of adhesive bonds [71], as well as composites in order to describe the bonding between fibers and matrix. Especially for CMCs, which can be assigned to the subgroup of composites with a weak-matrix interface, the description of the interface between fiber and matrix is important. Due to the low bonding strength of fiber and matrix, it can be observed that cracking in the matrix propagates around the fibers and continues along the interface (cf. Fig. 29, right) [1]. The CZM can reproduce this behavior numerically (cf. Fig. 29, left) and thus contributes an important part to the reproducibility of the real behavior.

The description can be done via the so-called cohesive-traction law. Models commonly used to describe the fiber-matrix interface are the linear cohesive-traction law and the bi-linear cohesive traction law.

The bilinear cohesive traction approach can be divided into two parts: The linear-elastic part and the damaged part with linear softening. If a defined maximum traction is exceeded at a defined displacement δ_0, the linear-elastic region ends and, according to the so-called 'linear decay law', a linear, irreversible decrease in the strength of the affected zone region at increasing strain starts until the traction of the element is no longer sufficient and a local separation of the bonded materials occurs. At this point the crack is considered fully developed. The behavior is shown in Fig. 30 [73].

In the linear-elastic region, the stiffness parameter K can be used to infer the coherent displacement at the contact surface. Provided the maximum traction of the material is not exceeded, the contact between the elements remains intact. This relationship for the different load types (Mode I, II and III) will be described as follows:

$$T^L = \begin{bmatrix} T_s \\ T_t \\ T_n \end{bmatrix} = \begin{bmatrix} K & 0 & 0 \\ 0 & K & 0 \\ 0 & 0 & K \end{bmatrix} \begin{bmatrix} \delta_s \\ \delta_t \\ \delta_n \end{bmatrix} \tag{23}$$

whereas.

T_s: Traction in shear direction (Mode II)
T_t: Traction in tangential direction (Mode III)
T_n: Traction in normal direction (Mode I)
K: Stiffness parameter
$\delta_{s;t,n}$: Associated displacements
T^L: Stress tensor for linear-elastic region

If the material is stressed beyond the elastic range, damage initiation in the material begins with the help of the so-called mixed-mode quadratic nominal stress criterion:

$$\left\{\frac{\langle T_n \rangle}{T_{n,0}}\right\}^2 + \left\{\frac{T_s}{T_{s,0}}\right\}^2 + \left\{\frac{T_t}{T_{t,0}}\right\}^2 = \left\{\frac{\frac{1}{2}(T_n + |T_n|)}{T_{n,0}}\right\}^2 + \left\{\frac{T_s}{T_{s,0}}\right\}^2 + \left\{\frac{T_t}{T_{t,0}}\right\}^2 = 1 \tag{24}$$

whereas.

$T_{n0,s0,t0}$: Strengths of the material for the respective mode
$\langle T_n \rangle$: Normal force with Macaulay brace $\frac{1}{2}(T_n + |T_n|)$.

One special feature can already be derived from the criterion at this point: Compression of the contact surface alone cannot cause failure of the geometry. The damage parameter D can be defined via the Mode-I-based damage evolution law:

$$D = \frac{\delta_{n,f}\left(\delta_{n,max} - \delta_{n,0}\right)}{\delta_{n,max}\left(\delta_{n,f} - \delta_{n,0}\right)} \tag{25}$$

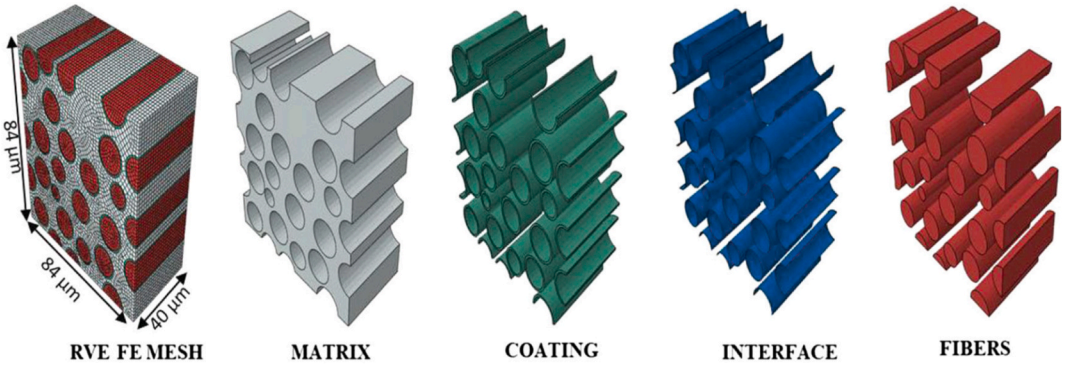

Fig. 27. General structure of a microscale model for fiber composites [64].

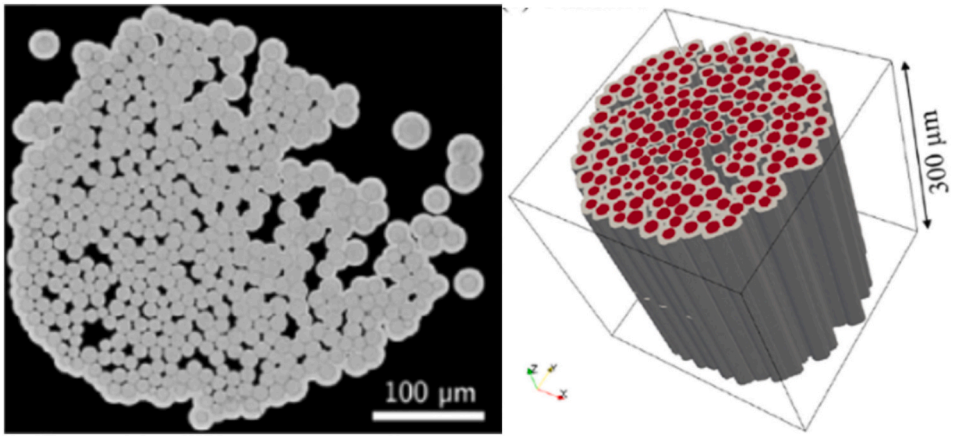

Fig. 28. CT image of a UD SiC/SiC (left) [65] as well as the re-modelling [66].

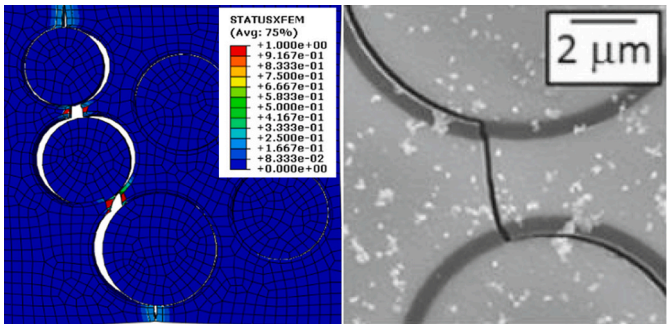

Fig. 29. Failure of the numerical microstructure of a SiC/SiC composite material with BN interface (left), SEM image of the crack propagation in the material (right) [72].

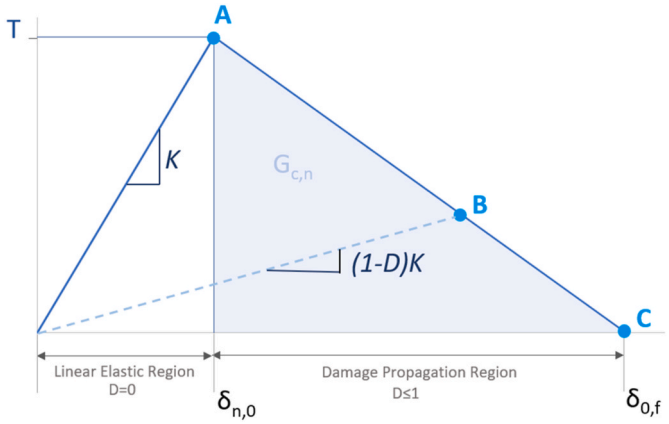

Fig. 30. Bi-linear traction separation law for the cohesive surface approach.

whereas.

$\delta_{n,max}$: Maximum displacement for Mode-I normal load
$\delta_{n,0}$: Displacement (Mode I) at D = 0
$\delta_{n,f}$: Displacement (Mode I) with D = 1

The displacement at complete failure of the structure can be derived from the following relationship:

$$\delta_{n,f} = \frac{2G_{c,n}}{T_{n,0}} = \frac{2G_{c,n}}{K\delta_{n,0}} \tag{26}$$

whereas.

$\mathbf{G_{c,n}}$:Critical fracture energy

In summary, the regions with and without damage can be described for their respective elements with the following equation:

$$\tau = \begin{cases} T^L & \delta_{n,max} \leq 0 \\ (1-D)K\delta_i, with\ i = n,s,t;\ \delta_{n,max} > 0 \end{cases} \tag{27}$$

4.3. Application in the machining process of fiber reinforced plastics

For the application to the machining process of composites, the aspects of geometry modelling, brittle material models and the cohesive zone model presented in the previous sections are applied. In their work [74], dealt with the numerical investigation of different fiber orientations of unidirectional carbon fiber reinforced plastic for micro as well as macro models. The micro model is implemented by modelling the fibers with a brittle fracture model, the matrix via an isotropic elastic-plastic material model, with the interface combined via the cohesive zone model. Whereas the macro model is implemented with the 3D Hashin theory. Rong et al. validated these results with a series of tests for the individual fiber orientations. In addition to chip formation, the damage to the machined surface (cf. Fig. 31, right) was compared using SEM and machining forces. The machining forces show very good agreement for all methods presented with a maximum deviation of 2 N for the respective methods.

Analogous to the procedure of [74,75] investigated the machining forces for CFRP using 2D simulation macromodel according to Hashin and a micromodel using the Cohesive Zone Model. The machining forces and the removal mechanism via high-speed cameras were used for validation. For a fiber orientation of 90°, Fig. 32 shows a general agreement of the different methods. For a fiber orientation of 90°, the largest investigated variation in machining force is shown by experiment (55 N), microsimulation (35 N) and macrosimulation (47.5 N).

The comparability of the macro and micro methods is illustrated in Fig. 33. Chip formation occurs between the two methods with only minor differences.

The different approaches between the 2D [75] and 3D simulation [74] show different degrees of deviations in the processing force. Simplifying to 2D space reduces the complexity of the model and, at the same time, the comparability to the real model. If the random fiber orientation in space is considered, the fracture behavior of the material changes depending on the positioning of individual fibers and thus the resulting machining force. It is therefore necessary for 3D simulations to consider a random distribution of fibers in space in order to produce results that are as close to reality as possible [76]. For 2D simulations, an

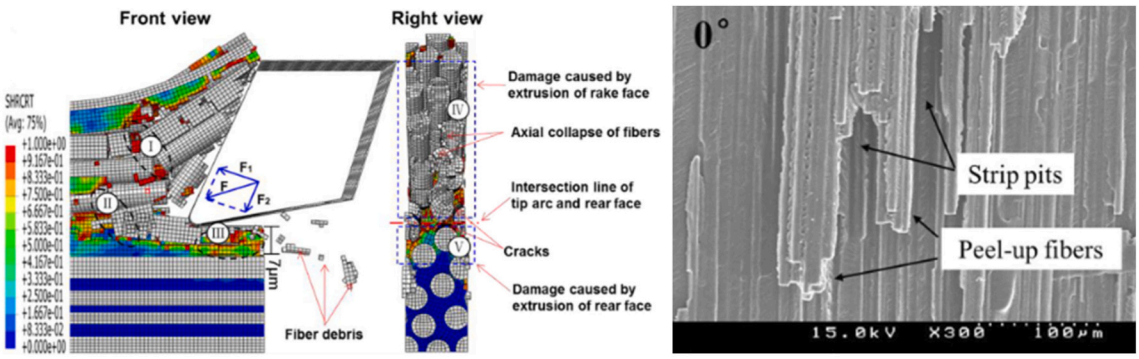

Fig. 31. Microscale simulation of the machining process of CFRP with 0° fiber orientation: machining simulation (left), resulting real surface after machining (right) [74].

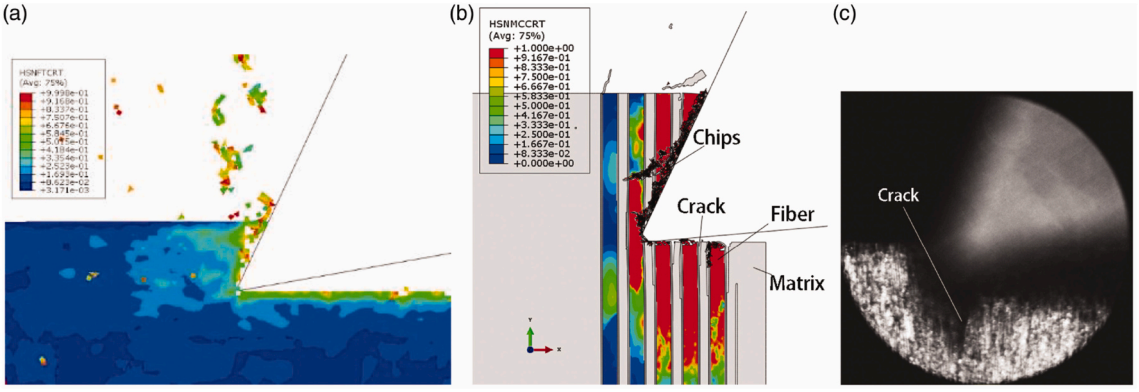

Fig. 32. Removal process for a 90° fiber orientation of CFRP via (a) macroscopic simulation, (b) microscopic simulation, c) experiment [75].

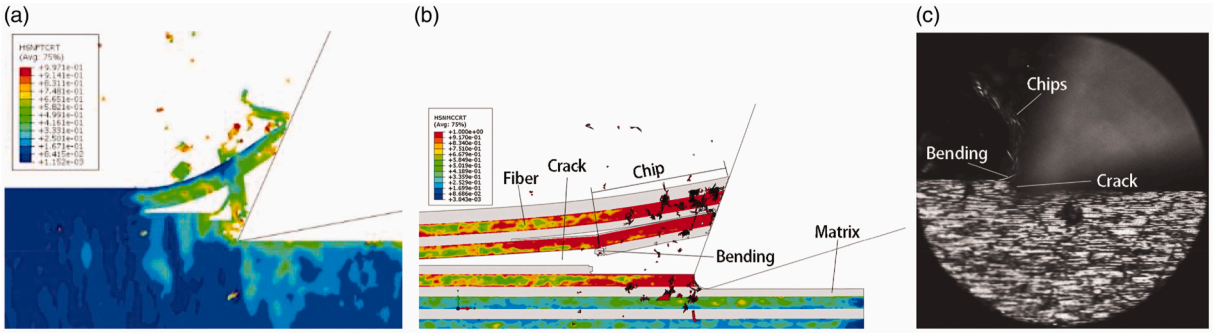

Fig. 33. Removal process for a 135° fiber orientation of CFRP via (a) macroscopic simulation, (b) microscopic simulation, and (c) experiment [75].

error results from an idealized distribution of fibers outside the considered plane, nevertheless it can be proven over a large number of studies that a simulation in 2D space is a useful first step for the modelling of fiber composite materials. Especially the saving of computation time is a significant advantage that can be used for the prediction of a 3D model.

Table 5 shows a selection of different works from recent years for composites, mostly CFRP. The methods for modelling and validation of micro and macro models presented in the previous papers are almost constant in the research environment.

5. Application to the machining simulation of ceramic matrix composites

Based on the previously presented results of the state of the art, a machining simulation for CMC will be derived. The principles for modelling the machining process of CFRP and the geometry modelling of CMC will be used. The objective is to transfer the knowledge gained from the areas of monolithic ceramics and fiber-reinforced plastics to the more complex case of machining of CMCs. In the following, the structure of the numerical simulation will be described in more detail, followed by a comparison with existing experimental test series.

Table 5
Application examples for the machining of fiber composites.

Source	Material (material model)	Machining process	Validation
[77]	C/SiC (C-fiber: Maximum stress failure criterion, SiC: JH2, Interface: traction separation criterion)	Orthogonal cutting/Milling	Comparison between SEM surface after machining and removal mechanisms in FEM
[78]	C/C-UD (Macro model: Jones-Nelson-Theory, Hashin-Chang-Criteria)	Orthogonal cutting	Comparison of forces (test series and simulation)
[79]	CFK-UD, 2D (Hashin)	Orthogonal cutting	Surface analysis (SEM and test series)
[80]	C/C-DU (Macromodel: Multiscale approach)	Orthogonal cutting	Comparison of forces (test series and simulation)
[81]	CFK-UD, 3D (Cohesive Zone, Hashin)	Orthogonal cutting	Comparison of forces (test series and simulation), $\Delta F \leq 10\%$.
[74]	CFK-UD, 3D (Micro model: Brittle Fracture; Cohesive Zone) (Macro model: Hashin)	Orthogonal cutting	Comparison of forces (test series and simulation, micro and macro model respectively) $\Delta F < 2$ N (below 10%), examination of the surface (SEM and test series)
[76]	CFK-UD, 3D (Cohesive Zone, elasto-plastic shear-lag approach: Weibull distribution + Monte-Carlo-method for strength of fiber)	Orthogonal cutting	Surface analysis (SEM and test series)
[75]	CFK-UD, 3D (Micro model: Brittle Fracture; Cohesive Zone) (Macro model: Hashin)	Orthogonal cutting	Comparison of forces (Test series and simulation, micro and macro model respectively) $\Delta F \approx 10$–20 N (up to 20%)
[82]	Macro model: Hashin	Drilling	Comparison of edge quality, machining forces (test series and simulation)

5.1. Numerical and experimental setup

A CVI (Chemical Vapor Deposition) SiC/SiC material from the company BJS Composites GmbH is selected for the simulation of the machining process. The modelling of the geometry is performed by considering the microstructure, taking into account the average fiber, pore and matrix content of the material as well as the size distribution of the fibers. For this purpose, a script in the software Matlab is developed, which derives a statistically representative geometry based on evaluations of micrographs of the SiC/SiC microstructure. The microstructure has a porosity of 8%, a fiber content of 57% and a matrix content of 35%. The aim of the geometry model is to represent the microstructure as realistically as possible to be able to depict possible machining phenomena, such as notch effects caused by porosity. Fig. 34 a) shows the structure of the numerical model, the derived microstructure with a size of 500x100 × 100 µm is shown in Fig. 34, b). A height of 100 µm is chosen to reduce computation time. Orthogonal cutting is used in this experimental set-up, so the tool is defined as 30 µm wider than the workpiece on both sides at the edge to exclude unwanted effects at the edge zones. The tool has a rake and clearance angle of 10°, and an edge radius of 20 µm. The depth of cut is 32 µm.

For the assignment of matrix and fibers, the JH1 model from Ref. [21] is used, which according to Ref. [83] is better suited for the silicon carbide than the JH2 material model. Since the JH1 model is already implemented in most software products compared to the JHB material model, which is optimized for SiC, the JHB model is intentionally not used. It is therefore to be expected that an improvement of the numerical model can be achieved by considering the JHB model in the future. Based on the data of [84,85] an erosion criterion for the failure strain (FS) of 0.3 is used for the material matrix. For Hi-Nicalon fiber, a FS of 1.0 is used based on values from Ref. [86]. The maximum failure strain of the fibers is calculated for each fiber with a percentage variation according to the data of [87]. For the definition of the interface, a tiebreak contact between fiber and matrix is defined instead of the CZM. These are upper limits in the shear and normal directions, beyond which local contact separation occurs. This simplification compared to the cohesive zone model serves to reduce the complexity of the model. For the strength of the interface, different maximum values between 50 and 100 MPa are found, depending on the coating type [72,88]. Since the strength of the interface depends on the coating thickness according to Ref. [89], the maximum strength in the shear and normal directions with 75 MPa is used.

The experiment is analogous to the setup in Fig. 34. To enable a stable and reproduceable experiment, the depth of cut is repeatedly calibrated to + -1 µm accuracy via a calibration prism. The alignment between tool and component is reproduced with +-0.01° accuracy. To reduce any possible damage to the surface of the component and to align the surface as well as possible to the tool coordinate system, the component is carefully polished in advance using a mounted point with a grain size of D46 before calibration process is performed. Before the test, the width of the component is determined with +-5 µm accuracy, as the machining force will be referenced to the component width to

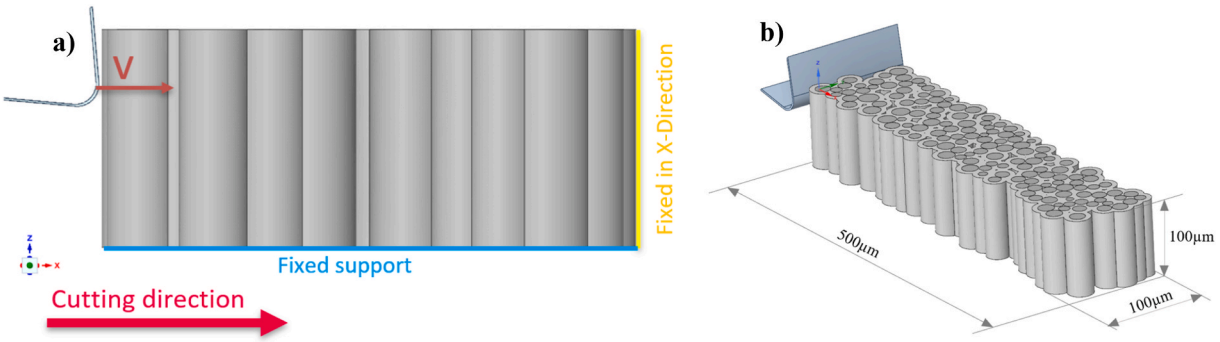

Fig. 34. a) Definition of boundary conditions for the simulation, b) Structure of the microgeometry.

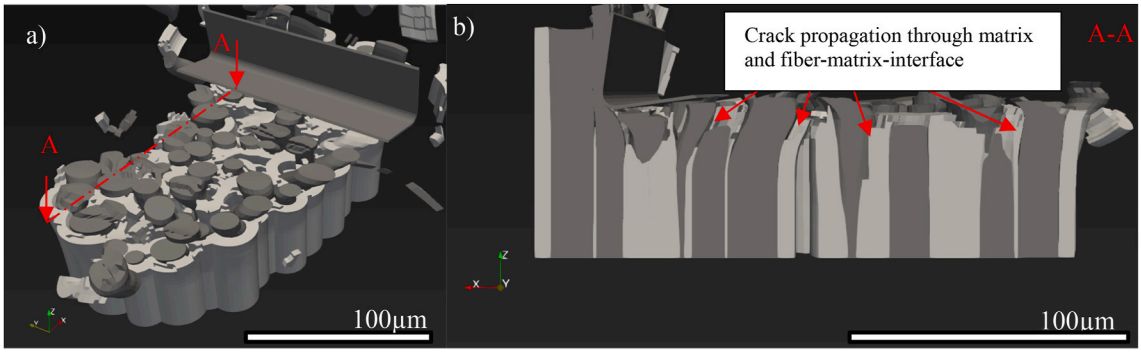

Fig. 35. a) 3D view of the machining simulation, b) section cut of the material.

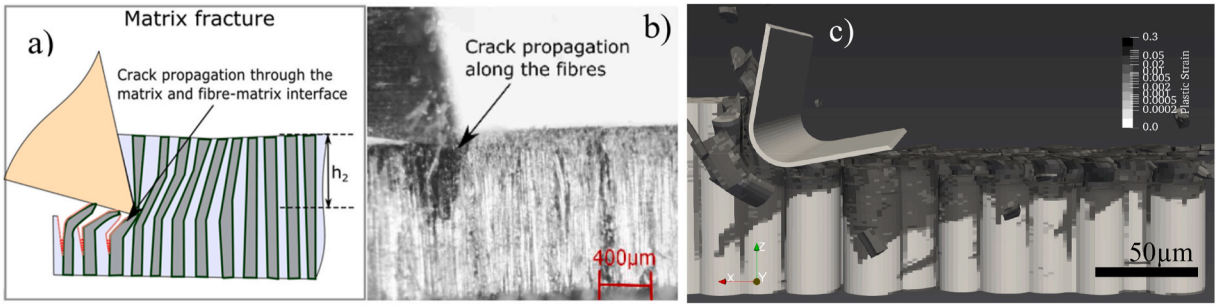

Fig. 36. a) Schematic representation of the matrix fracture phenomenon when machining with a fiber orientation angle of 90°, b) High speed image during machining with a fiber orientation angle of 90° with orthogonal cutting of C/C [20] and c) observable damage visualized through plastic strain in the machining simulation.

compare to the simulation. The material is attached to a load cell, which measures with a frequency of 100 kHz.

5.2. Discussion of results

The machining simulation demonstrates the expected brittle removal behavior when machining perpendicular to the fiber direction at a depth of cut of 32 µm, whereby a separation of the bonding of fiber and matrix and thus a crack propagation in depth can be observed (cf. Fig. 35). In the case of this simulation, no fiber pullout can be observed because the fibers at the bottom end are defined as a fixed support. Due to the strong bending of the fibers and the associated breaking of the interface into depth, in some cases up to complete depth of the part, it can be assumed that a fiber pull-out will take place under alternative boundary conditions.

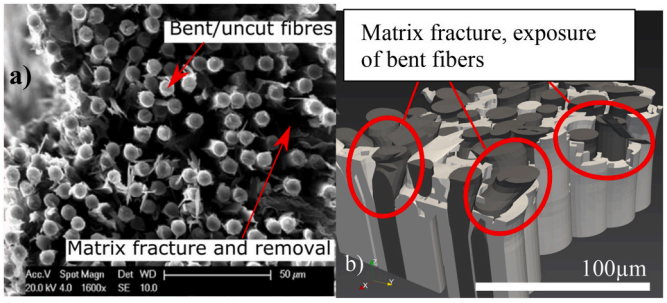

Fig. 37. SEM analysis of the machined surface for brittle cutting in transverse fibers of C/C [20] a) and simulated surface of CVI SiC/SiC b).

According to Ref. [20], the matrix fracture observed in this simulation occurs when the shear stress applied by the cutting tool cannot achieve the maximum shear stress of the composite. This is shown in Fig. 36, a) as a schematic representation, as an experiment by orthogonal cut in Fig. 36, b) and in the simulation showing the plastic strain in, which, according to formula (8), directly relates to the accumulated damage (cf. Fig. 36 c)).

When comparing the simulated surface (cf. Fig. 37, b)) and the experimental surface of the C/C material from (Diaz 2017) (cf. Fig. 37, a)), parallelisms in the machining mechanism can be identified. In both cases, it can be observed that the fibers are stretched more due to the higher elasticity and are therefore not damaged as much as the matrix. Compared to the carbon fibers in Diaz's experiment, SiC fibers have lower elasticity and the SiC matrix a higher strength, which makes this effect more readily distinct in the simulation, so as expected. Furthermore, a higher cutting depth was applied in the experiment, which also amplifies the effect shown. Nevertheless, the shown machining operations show a similar removal pattern.

Fig. 38 shows the force curve in the cutting direction for a maximum tension of the tiebreak contact of 75 MPa as well as the mean thereof, from experiment and simulation. To obtain comparability between the experimental and simulated force values, the machining force was related to the sample width (experimental 2 mm, simulation 0.1 mm). Furthermore, the available data from simulation and experiment are related to their absolute machining length to obtain a standardized side-by-side comparison of the two processing paths. This allows for a comparison of fluctuations occurring from simulation and experiment and, thus, recurring machining patterns can be identified. The mean value of the force related to the component width is in good agreement with the experimental data of [90]. The force curve can be used to see how much of the material is currently engaged in the cutting process. A sudden

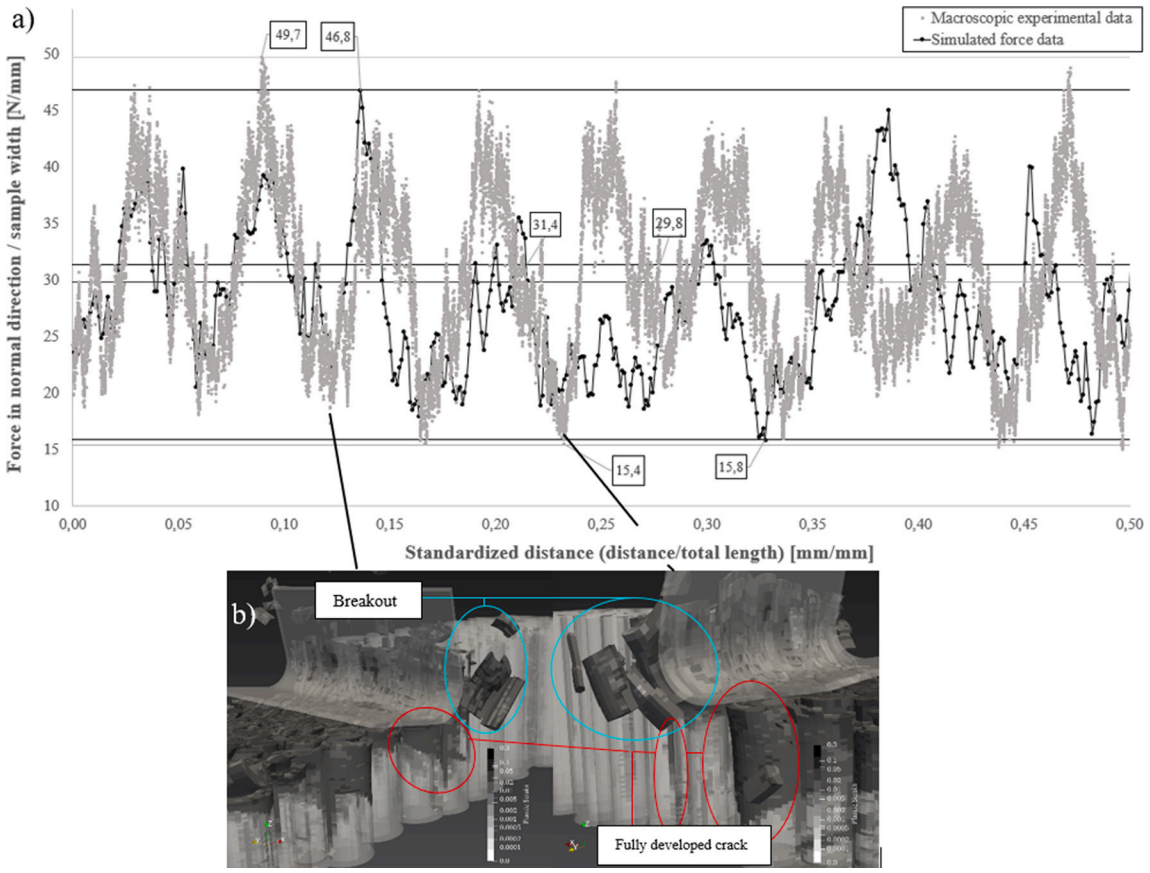

Fig. 38. a) Simulated machining force per sample width and average simulation and experimental data over time, b) examples of breakout points leading to a force drop.

drop in force can be recognized with the breakage of the material in both matrix and fiber. This is shown in Fig. 38 b). Small drops in the force curve indicate the erosion of smaller pieces of the matrix or interface. Greater reductions in force are observed when either larger pieces of the matrix are broken out at open surfaces caused by the porosity of the material, or when fibers are removed and larger cracks into the material are formed (cf. Fig. 38 b)).

Fig. 38 a) shows that both maxima (46.8 N/mm simulation and 49.7 N/mm experiment) and minima (15.8 N/mm simulation and 15.4 N/mm experiment) are in very good agreement. The mean values of 31.4 N/mm in the experiment and 29.8 N/mm in the simulation also show clear agreement between the data. Through the standardized consideration of the distance covered, it is evident that both experimentally and simulatively a recurring increase and decrease of the force occurs. This can be attributed to the previously described events. Using the simulation at these data points, it is possible to examine this behavior in more detail. It can be observed that both the formation of larger crack systems and the breakout of material occur superimposed and lead to these force drops in the simulation. Both frequency and height of the force peaks are generally in agreement in simulation and experiment, although the force peaks of the simulation show a not so uniform recurring strength of the force peak. In addition, the simulation shows a slight deviation in frequency compared to the experiment. The high machining forces of the experiment indicate that the orthogonal cutting method is not well suited for machining SiC/SiC as such. Nevertheless, by simplifying the kinematics of the process, a better understanding of the material removal mechanisms can be developed, especially in the field of simulation. For a more detailed analysis of this experiment please refer to the paper by Ref. [90]. Here, an identical experimental setup was used, and the experimental aspect was examined more in-depth.

In addition to occurring forces, the surface roughness of the material can be compared to obtain a comparison between simulation and experiment. For the simulated surface and the surface determined by experiment, three height categories are introduced. Those are subdivided into the categories 'high' 'medium' and 'low'. 'High' refers to the height range of the surface between 10,1 and 6,6 µm, 'medium' between 6,6 and 3,3 µm and 'low' from 3,3 to 0 µm of the surface. Fig. 39 a), shows a surface image of the machined surface, Fig. 39 b) the simulated surface and its height distributions.

Due to the limitation of the simulatable element height, a more developed height profile in the range between 10,1 and 6,6 µm is visible in the simulation. It underrepresents the area between 3,3 and 6,6 µm statistically. In both cases, it is visible that, as expected, a multitude of bent fibers are exposed. In both surfaces, areas can be observed where the matrix has a similar height to the fibers (Fig. 39, a) and b), orange-red area). Furthermore, it can be seen that in the region around the porosity of the material (shown as dark blue in Fig. 39 a), and cyan-dark blue in Fig. 39 b)), the matrix is broken out and thus not at the same height level as the matrix in the orange region in both surfaces. This effect is to be expected due to the notch effect at the edge zones between material and pore. Thus, to describe this effect in simulation, the porosity was considered in the geometry modeling from the beginning. Due to the simplification in geometry modeling of the porosity, the porosity is represented significantly deeper than it appears in the experiment. If the porosity in the geometry model is modeled by closed porosity, as in reality, an even clearer comparability of the surfaces in

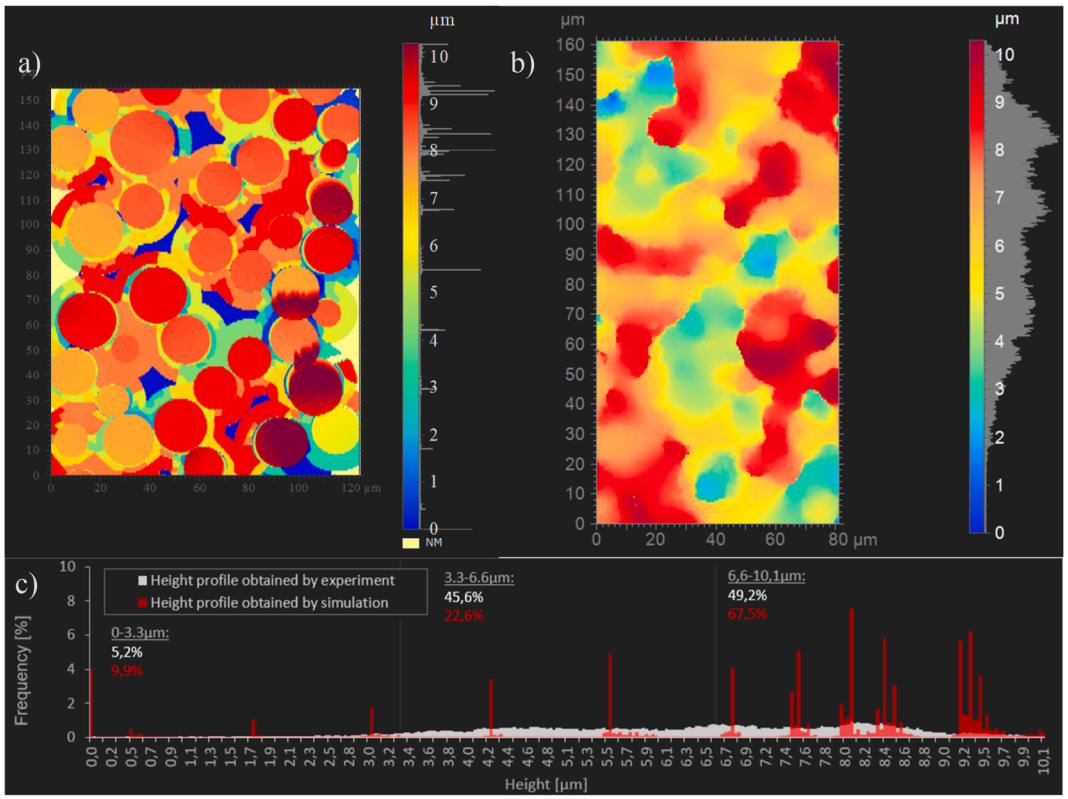

Fig. 39. Machined surfaces obtained by simulation a) and experiment b) along with their height distribution in histogram form c).

the deeper areas is possible. To achieve a better correlation of the surfaces, a reduced element height is needed to display crack propagation into the depth of the material more precisely. Nevertheless, both the simulated and experimentally determined surfaces show clear similarities. The height differences between the lowest and highest points are the same in both surfaces, which means that a reasonable approximation to reality has already been achieved. Moreover, an identical distribution would never be likely, since the exact surface roughness will always vary depending on local pre-damage, fiber strength and other parameters during the manufacturing of the component. However, since both data sets show general agreement both visually and in data location, it can be concluded that the model can predict the roughness with acceptable accuracy at a sufficient resolution.

Since the experimental setup is not a unidirectional CVI SiC/SiC but a woven fabric, deviations due to the structural design are to be expected. Further simplifications such as the frictionless contact between tool and component also influence the machining force and surface roughness. Nevertheless, it can be concluded that the presented methodology for simulating the cutting process by microstructural simulation of the CVI SiC/SiC material shows a good approximation to reality.

6. Conclusion and outlook

In this work, methods and approaches for the simulation of brittle-hard monolithic ceramic materials were presented. For the finite element analysis, the Johnson-Holmquist 2 model was presented, as well as the discrete element method and smooth particle hydrodynamics. Furthermore, the advantages and disadvantages of the individual methods for machining simulation were examined in more detail.

1) FEA is well suited for continuous processes but, due to large deformation of elements and the high resolution required to adequately describe crack propagation, it is not as efficient in determining non-continuous processes such as crack propagation during machining compared to the other methods presented.
2) SPH and DEM are suited for processing highly discontinuous events such as machining, as crack propagation between particles can be achieved more efficiently.
3) Selective coupling of discontinuous methods (SPH, DEM) with continuous methods (FEM) allows for a significant saving of computational time with the same precision of results, provided that a reasonable partitioning is made.

In addition, basic principles for the machining of composite materials were presented. The following key statements were derived.

1) Composite materials are subdivided into different scales for machining processes due to their anisotropy, and each of these scales focuses on specific geometric features of the material.
2) The microscale provides the most accurate information regarding the removal and damage behavior of these materials for very small individual areas of the material.
3) Consideration of the microscale is particularly useful for brittle-hard composites such as CMCs, where microporosity has an influence on machinability.
4) The direction of the fibers relative to the cutting edge determines the damage mechanisms that occur.
5) Depending on the applied shear force of the tool, different damage mechanisms can occur in relation to the strength of the component, which can be traced by fiber-matrix interface, matrix, or total strength.

Additionally, the Cohesive Zone Model was presented to describe the fiber-matrix bonding.

1) The fiber-matrix bonding is described in the literature via the CZM, whereby different modes can be considered or neglected.
2) For machining, mainly Mode I and Mode II loads occur.

3) Besides composites such as CFRP, the CZM can also be used for brittle materials such as CMCs.

SPH and FEA use the same underlying models, which means that the coupling of the two methods can take advantage of each other. This is particularly interesting for brittle-hard materials such as CMCs, for which crack propagation through the weak fiber-matrix interface can be expected in addition to the formation of fractures in the brittle-hard matrix.

Furthermore, approaches for the simulation of CFRP using the material models of ceramics were adopted to simulate the machining process of CVI SiC/SiC. A geometry model was created considering the microstructure with statistical distributions such as porosity, fiber, and matrix content as well as fiber size distribution. The following data was derived by comparing the results with the experiment.

1) The average simulated machining force per sample width is 29.8 N/mm and in the experiment 31.4 N/mm.
2) The maximum machining force per sample width of the simulation is 46.8 N/mm, in the experiment 49.7 N/mm. The minimum forces per part width are 15.8 N/mm (simulation) and 15.4 N/mm (experiment). The simulated data therefore is in good agreement with the experimental determined data.
3) Large force drops of the simulation can be assigned to failure points in which a large breakout occurs for the microscale.
4) The increase and decrease of forces occur in a recurring pattern in the experiment, which is also well reflected in the simulation, considering certain alterations.
5) The resulting surface of the simulation shows the removal characteristics presented by Ref. [20], but not as distinct for the SiC/SiC material presented.
6) Furthermore, the surfaces from simulation and experiment were compared. It could be shown that the simulated surface in the height range between 6,6 and 10,1 μm (67,5%) is more distinct than in the experiment (49,2%), while the medium height range between 3,3 and 6,6 μm were less distinct (22,6% simulation, 45,6% experiment). Lower ranges between 0 and 3,3 μm were in good agreement with 9,9% in Simulation and 5,2% in the experiment.
7) It could be shown that the matrix in the proximity of microporosity is more broken out than at other locations in both experiment and simulation, creating a heigh profile of 10 μm in both simulation and experiment.

The proposed model shows good agreement with experimental data despite simplifications. The objective of future work is therefore the adaptation and optimization of the presented research to the machining of CMC materials. Thus, the complex removal mechanisms of these materials can be better understood.

Declaration of competing interest

The authors declare that they have no known competing financial interests or personal relationships that could have appeared to influence the work reported in this paper.

Acknowledgements

This research did not receive any specific grant from funding agencies in the public, commercial, or not-for-profit sectors.

References

[1] K. Detwiler, R. Hunt, E. Opila, In-situ observation of micro-cracking in a SiC/BN/SiC ceramic matrix composite under tension, Open Ceram. 14 (2023), 100366.
[2] C. Yang, S. Wu, S. Wu, X. Liu, Z. Zhao, In-situ characterization on crack propagation behavior of SiCf/SiC composites during monotonic tensile loading, J. Eur. Ceram. Soc. 42 (15) (2022) 6836–6845.
[3] F. Cepero-Mejías, J.L. Curiel-Sosa, A. Blázquez, T.T. Yu, K. Kerrigan, V.A. Phadnis, Review of recent developments and induced damage assessment in the modelling of the machining of long fibre reinforced polymer composites, Compos. Struct. 240 (2020), 112006.
[4] J. Du, M. Geng, W. Ming, W. He, J. Ma, Simulation machining of fiber-reinforced composites: a review, Int. J. Adv. Des. Manuf. Technol. 117 (1–2) (2021) 1–15.
[5] J. Jiao, X. Cheng, J. Wang, L. Sheng, Y. Zhang, J. Xu, et al., A review of research progress on machining carbon fiber-reinforced composites with lasers, Micromachines 14 (1) (2022).
[6] J. Mackerle, Finite element analysis and simulation of machining: an addendum, Int. J. Mach. Tool Manufact. 43 (1) (2003) 103–114.
[7] S. Rawal, A.M. Sidpara, J. Paul, A review on micro machining of polymer composites, J. Manuf. Process. 77 (2022) 87–113.
[8] N. Shetty, S.M. Shahabaz, S.S. Sharma, S. Divakara Shetty, A review on finite element method for machining of composite materials, Compos. Struct. 176 (2017) 790–802.
[9] Y. Song, H. Cao, W. Zheng, Da Qu, L. Liu, C. Yan, Cutting force modeling of machining carbon fiber reinforced polymer (CFRP) composites: a review, Compos. Struct. 299 (2022), 116096.
[10] L. Zhang, Z. Wu, C. Wu, Q. Wu, On the numerical modelling of composite machining, Compos. B Eng. 241 (2022), 110023.
[11] J. Du, H. Zhang, Y. Geng, W. Ming, W. He, J. Ma, et al., A review on machining of carbon fiber reinforced ceramic matrix composites, Ceram. Int. 45 (15) (2019) 18155–18166.
[12] S. Jiang, C. Tang, X. Li, Y. Tan, R. Peng, D. Yang, S. Liu, Discrete element modeling of the machining processes of brittle materials: recent development and future prospective, Int. J. Adv. Des. Manuf. Technol. 109 (9–12) (2020) 2795–2829.
[13] S.M.T.I. Nayim, M.Z. Hasan, A. Jamwal, S. Thakur, S. Gupta, Recent trends & developments in optimization and modelling of electro-discharge machining using modern techniques: a review, in: AIP Conference Proceedings, 1ST INTERNATIONAL CONFERENCE on ADVANCES IN MECHANICAL ENGINEERING and NANOTECHNOLOGY (ICAMEN 2019), AIP Publishing, 2019, 30051.
[14] P. Parandoush, A. Hossain, A review of modeling and simulation of laser beam machining, Int. J. Mach. Tool Manufact. 85 (2014) 135–145.
[15] Z. Wang, Y. Cai, X. Luo, Modelling and simulation of cutting process by smoothed particle hydrodynamics (SPH): a review, in: 2019 25th International Conference on Automation and Computing (ICAC), IEEE, 2019, pp. 1–6.
[16] L. Zhao, J. Zhang, J. Zhang, H. Dai, A. Hartmaier, T. Sun, Numerical simulation of materials-oriented ultra-precision diamond cutting: review and outlook, Int. J. Extrem. Manuf. 5 (2) (2023), 22001.
[17] A.P. Markopoulos, Cutting mechanics and analytical modeling, in: A. P. Markopoulos (Ed.), SpringerBriefs in Applied Sciences and Technology. Finite Element Method in Machining Processes, Springer London, London, 2013, pp. 11–27.
[18] V.P. Astakhov, S.V. Shvets, A system concept in metal cutting, J. Mater. Process. Technol. 79 (1–3) (1998) 189–199.
[19] Z. Liao, D.A. Axinte, On chip formation mechanism in orthogonal cutting of bone, Int. J. Mach. Tool Manufact. 102 (2016) 41–55.
[20] O. Gavalda Diaz, D.A. Axinte, Towards understanding the cutting and fracture mechanism in Ceramic Matrix Composites, Int. J. Mach. Tool Manufact. 118–119 (2017) 12–25.
[21] G.R. Johnson, T.J. Holmquist, An improved computational constitutive model for brittle materials, in: AIP Conference Proceedings, AIP, 1994, pp. 981–984.
[22] J. Wang, Y. Yin, C. Luo, Johnson–Holmquist-II(JH-2) constitutive model for rock materials: parameter determination and application in tunnel smooth blasting, Appl. Sci. 8 (9) (2018) 1675.
[23] Y. Gu, Y. Zhou, J. Lin, A. Yi, M. Kang, H. Lu, Z. Xu, Analytical prediction of subsurface damages and surface quality in vibration-assisted polishing process of silicon carbide ceramics, Materials 12 (10) (2019).
[24] H. Pen, J. Guo, Z. Cao, X. Wang, Z. Wang, Finite element simulation of the micromachining of nanosized-silicon-carbide-particle reinforced composite materials based on the cohesive zone model, Nanotechnol. Prec. Eng. 1 (4) (2018) 242–247.
[25] Y. Gu, W. Zhu, J. Lin, M. Lu, J. Sun, Investigation of silicon carbide ceramic polishing by simulation and experiment, Adv. Mech. Eng. 9 (11) (2017), 168781401772909.
[26] D. Zhu, S. Yan, B. Li, Single-grit modeling and simulation of crack initiation and propagation in SiC grinding using maximum undeformed chip thickness, Comput. Mater. Sci. 92 (2014) 13–21.
[27] P.A. Cundall, O.D.L. Strack, A discrete numerical model for granular assemblies, Geotechnique 29 (1) (1979) 47–65. https://doi.org/10.1680/geot.1979.29.1.47.
[28] L.A.M. Camones, E.d.A. Vargas, R. P. de Figueiredo, R.Q. Velloso, Application of the discrete element method for modeling of rock crack propagation and coalescence in the step-path failure mechanism, Eng. Geol. 153 (2013) 80–94.
[29] H. Huang, B. Lecampion, E. Detournay, Discrete element modeling of tool-rock interaction I: rock cutting, Int. J. Numer. Anal. Methods GeoMech. 37 (13) (2013) 1913–1929.
[30] S. Hentz, F.V. Donzé, L. Daudeville, Discrete element modelling of concrete submitted to dynamic loading at high strain rates, Comput. Struct. 82 (29–30) (2004) 2509–2524.
[31] W. Gao, M. Zang, The simulation of laminated glass beam impact problem by developing fracture model of spherical DEM, Eng. Anal. Bound. Elem. 42 (2014) 2–7.
[32] M.Y. Zang, Z. Lei, S.F. Wang, Investigation of impact fracture behavior of automobile laminated glass by 3D discrete element method, Comput. Mech. 41 (1) (2007) 73–83.

[33] S. Jiang, X. Li, Y. Tan, H. Liu, Z. Xu, R. Chen, Discrete element simulation of SiC ceramic with pre-existing random flaws under uniaxial compression, Ceram. Int. 43 (16) (2017) 13717–13728.

[34] Y. Liu, J. Deng, Machining process modeling of green alumina ceramics in orthogonal cutting and fragmentation process, Int. J. Adv. Des. Manuf. Technol. 113 (3–4) (2021) 1009–1027.

[35] A.P. Roberts, E.J. Garboczi, Elastic properties of model porous ceramics, J. Am. Ceram. Soc. 83 (12) (2000) 3041–3048.

[36] Y. Tan, D. Yang, Y. Sheng, Study of polycrystalline Al2O3 machining cracks using discrete element method, Int. J. Mach. Tool Manufact. 48 (9) (2008) 975–982.

[37] G. Yang, H. Alkotami, S. Lei, Discrete element simulation of orthogonal machining of soda-lime glass with seed cracks, J. Manuf.Mater. Process. 4 (1) (2020) 5.

[38] Y. Wang, P. Mora, Macroscopic elastic properties of regular lattices, J. Mech. Phys. Solid. 56 (12) (2008) 3459–3474.

[39] D.V. Griffiths, G.G.W. Mustoe, Modelling of elastic continua using a grillage of structural elements based on discrete element concepts, Int. J. Numer. Methods Eng. 50 (7) (2001) 1759–1775.

[40] Y.-C. Wang, X.-C. Yin, F.-J. Ke, M.-F. Xia, K.-Y. Peng, Numerical simulation of rock failure and earthquake process on mesoscopic scale, in: P. Mora, M. Matsu'ura, R. Madariaga, J.-B. Minster (Eds.), PAGEOPH Topical Volumes. Microscopic and Macroscopic Simulation. Towards Predictive Modelling of the Earthquake Process, Birkhauser, Basel, 2001, pp. 1905–1928.

[41] S. Jiang, M. He, X. Li, C. Tang, J. Liu, S. Liu, Modeling and estimation of hole-type flaws on cracking mechanism of SiC ceramics under uniaxial compression: a 2D DEM simulation, Theor. Appl. Fract. Mech. 105 (2020), 102398.

[42] D. Iliescu, D. Gehin, I. Iordanoff, F. Girot, M.E. Gutiérrez, A discrete element method for the simulation of CFRP cutting, Compos. Sci. Technol. 70 (1) (2010) 73–80.

[43] Y. Tan, D. Yang, Y. Sheng, Discrete element method (DEM) modeling of fracture and damage in the machining process of polycrystalline SiC, J. Eur. Ceram. Soc. 29 (6) (2009) 1029–1037.

[44] R.A. Gingold, J.J. Monaghan, Smoothed particle hydrodynamics: theory and application to non-spherical stars, Mon. Not. Roy. Astron. Soc. 181 (3) (1977) 375–389.

[45] L.B. Lucy, A numerical approach to the testing of the fission hypothesis, Astron. J. 82 (1977) 1013.

[46] X. Dong, G. Hao, R. Yu, Two-dimensional smoothed particle hydrodynamics (SPH) simulation of multiphase melting flows and associated interface behavior, Eng. Appl. Comput. Fluid Mech. 16 (1) (2022) 588–629.

[47] T. Weaver, Z. Xiao, Fluid simulation by the smoothed particle hydrodynamics method: a survey, in: Proceedings of the 11th Joint Conference on Computer Vision, Imaging and Computer Graphics Theory and Applications, SCITEPRESS - Science and and Technology Publications, 2016, pp. 213–223.

[48] F. Spreng, P. Eberhard, Machining process simulations with smoothed particle hydrodynamics, Proc. CIRP 31 (2015) 94–99.

[49] J.W. Swegle, D.L. Hicks, S.W. Attaway, Smoothed particle hydrodynamics stability analysis, J. Comput. Phys. 116 (1) (1995) 123–134.

[50] N. Duan, Y. Yu, W. Wang, X. Xu, SPH and FE coupled 3D simulation of monocrystal SiC scratching by single diamond grit, Int. J. Refract. Metals Hard Mater. 64 (2017) 279–293.

[51] Y. Liu, B. Li, C. Wu, L. Kong, Y. Zheng, Smoothed particle hydrodynamics simulation and experimental analysis of SiC ceramic grinding mechanism, Ceram. Int. 44 (11) (2018) 12194–12203.

[52] B. Deng, M. Yang, L. Zhou, H. Wang, R. Yan, F. Peng, Smoothed particle hydrodynamics (SPH) simulation and experimental investigation on the diamond fly-cutting milling of zirconia ceramics, Proc. CIRP 82 (2019) 202–207.

[53] N. Ojal, H.P. Cherukuri, T.L. Schmitz, A.W. Jaycox, A comparison of smoothed particle hydrodynamics (SPH) and coupled SPH-FEM methods for modeling machining, in: In PROCEEDINGS OF THE ASME 2020 INTERNATIONAL MECHANICAL ENGINEERING CONGRESS AND EXPOSITION … (IMECE2020), 2A, Advanced manufacturing. [S.l.]: AMER SOC OF MECH ENGINEER, 2021.

[54] H. Song, P. Pan, G. Ren, Z. Yang, J. Dan, J. Li, et al., SPH/FEM modeling for laser-assisted machining of fused silica, Int. J. Adv. Des. Manuf. Technol. 106 (5–6) (2020) 2049–2064.

[55] X. Guo, Y. Wei, Z. Jin, D. Guo, W. Maosen, A numerical model for optical glass cutting based on SPH method, Int. J. Adv. Des. Manuf. Technol. 68 (5–8) (2013) 1277–1283.

[56] S. Koneshwaran, D.P. Thambiratnam, C. Gallage, Blast response of segmented bored tunnel using coupled SPH–FE method, Structures 2 (2015) 58–71.

[57] S. Swaddiwudhipong, M.J. Islam, Z.S. Liu, High velocity penetration/perforation using coupled smooth particle hydrodynamics-finite element method, Int. J. Prot. Struct. 1 (4) (2010) 489–506.

[58] S. Ceri, O. Bacarreza, Z.S. Khodaei, SPH, FEM and FEM-SPH numerical analysis of aluminium plate under low velocity impact, in: AIP Conference Proceedings, FRACTURE and DAMAGE MECHANICS: Theory, Simulation and Experiment, AIP Publishing, 2020, 20012.

[59] J. Das, H. Holm, On the improvement of computational efficiency of smoothed particle hydrodynamics to simulate flexural failure of ice, J. Ocean Eng. Mar. Energy 4 (2) (2018) 153–169.

[60] Z. Wang, Y. Lu, H. Hao, K. Chong, A full coupled numerical analysis approach for buried structures subjected to subsurface blast, Comput. Struct. 83 (4–5) (2005) 339–356.

[61] S.W. Attaway, M.W. Heinstein, J.W. Swegle, Coupling of smooth particle hydrodynamics with the finite element method, Nucl. Eng. Des. 150 (2–3) (1994) 199–205.

[62] S. Jiang, T. Li, Y. Tan, A DEM methodology for simulating the grinding process of SiC ceramics, Procedia Eng. 102 (2015) 1803–1810.

[63] R. Vacondio, C. Altomare, M. de Leffe, X. Hu, D. Le Touzé, S. Lind, et al., Grand challenges for smoothed particle hydrodynamics numerical schemes, Comput. Particle Mech. 8 (3) (2021) 575–588.

[64] S. Daggumati, A. Sharma, A. Kasera, N. Upadhyay, Failure analysis of unidirectional ceramic matrix composite lamina and cross-ply laminate under fiber direction uniaxial tensile load: cohesive zone modeling and brittle fracture mechanics approach, J. Mater. Eng. Perform. 29 (4) (2020) 2049–2060.

[65] C. Chateau, L. Gélébart, M. Bornert, J. Crépin, E. Boller, C. Sauder, W. Ludwig, In situ X-ray microtomography characterization of damage in SiCf/SiC minicomposites, Compos. Sci. Technol. 71 (6) (2011) 916–924.

[66] Y. Chen, J. Marrow, Effect of irradiation swelling on the mechanical properties of unidirectional SiC/SiC composites: a numerical investigation at microstructural level, J. Nucl. Mater. 569 (2022), 153918.

[67] C. Chateau, L. Gélébart, M. Bornert, J. Crépin, Micromechanical modeling of the elastic behavior of unidirectional CVI SiC/SiC composites, Int. J. Solid Struct. 58 (2015) 322–334.

[68] Y. Feng, J. Wang, N. Shang, G. Zhao, C. Zhang, J. Tang, et al., Multiscale modeling of SiCf/SiC nuclear fuel cladding based on FE-simulation of braiding process, Front. Mater. 7 (2021).

[69] D.S. Dugdale, Yielding of steel sheets containing slits, J. Mech. Phys. Solid. 8 (2) (1960) 100–104.

[70] G.I. Barenblatt, The mathematical theory of equilibrium cracks in brittle fracture, in: Advances in Applied Mechanics. Advances in Applied Mechanics, vol. 7, Elsevier, 1962, pp. 55–129.

[71] M. Lee, E. Yeo, M. Blacklock, M. Janardhana, S. Feih, C.H. Wang, Predicting the strength of adhesively bonded joints of variable thickness using a cohesive element approach, Int. J. Adhesion Adhes. 58 (2015) 44–52.

[72] S. Daggumati, A. Sharma, Y.S. Pydi, Micromechanical FE analysis of SiCf/SiC composite with BN interface, Silicon 12 (2) (2020) 245–261.

[73] Dassault Systemes Simulia, Inc. *ABAQUS, Analysis User's Manual.* .

[74] C. Rong, L. Shujian, L. Pengnan, L. Xiaopeng, Q. Xinyi, T.J. Ko, J. Yong, Effect of fiber orientation angles on the material removal behavior of CFRP during cutting process by multi-scale characterization, Int. J. Adv. Des. Manuf. Technol. 106 (11–12) (2020) 5017–5031.

[75] F. Wang, X. Wang, R. Yang, H. Gao, Y. Su, G. Bi, Research on the carbon fibre-reinforced plastic (CFRP) cutting mechanism using macroscopic and microscopic numerical simulations, J. Reinforc. Plast. Compos. 36 (8) (2017) 555–562.

[76] H. Liu, J. Lin, Y. Sun, J. Zhang, Micro model of carbon fiber/cyanate ester composites and analysis of machining damage mechanism, Chin. J. Mech. Eng. 32 (1) (2019).

[77] C. Liu, Z. Hou, L. Gao, R. Shen, Y. Li, Q. Zhou, Towards understanding the material removal mechanism in multi-tooth milling of 2.5D C/SiC composites: numerical modeling and experimental study, Int. J. Adv. Des. Manuf. Technol. 125 (9–10) (2023) 4163–4184.

[78] S. Zhang, Y. Li, M. Luo, C. Shan, Modelling of nonlinear and dual-modulus characteristics and macro-orthogonal cutting simulation of unidirectional Carbon/Carbon composites, Compos. Struct. 280 (2022), 114928.

[79] W. Wu, S. Li, X. Qin, W. Liu, X. Cui, H. Li, et al., Effects of fiber orientation on tool wear evolution and wear mechanism when cutting carbon fiber reinforced plastics, Chin. J. Aeronaut. (2022).

[80] C. Shan, M. Zhang, Y. Yang, S. Zhang, M. Luo, A dynamic cutting force model for transverse orthogonal cutting of unidirectional carbon/carbon composites considering fiber distribution, Compos. Struct. 251 (2020), 112668.

[81] H.N. Li, J.P. Wang, C.Q. Wu, Y.J. Zhao, J. Xu, X. Liu, W.Q. Zhu, Damage behaviors of unidirectional CFRP in orthogonal cutting: a comparison between single- and multiple-pass strategies, Compos. B Eng. 185 (2020), 107774.

[82] O. Isbilir, E. Ghassemieh, Finite element analysis of drilling of carbon fibre reinforced composites, Appl. Compos. Mater. 19 (3–4) (2012) 637–656.

[83] T.J. Holmquist, G.R. Johnson, Characterization and evaluation of silicon carbide for high-velocity impact, J. Appl. Phys. 97 (9) (2005), 93502.

[84] G.K. Sfantos, M.H. Aliabadi, A boundary cohesive grain element formulation for modelling intergranular microfracture in polycrystalline brittle materials, Int. J. Numer. Methods Eng. 69 (8) (2007) 1590–1626.

[85] V.I. Ivashchenko, P.E.A. Turchi, V.I. Shevchenko, Simulations of the mechanical properties of crystalline, nanocrystalline, and amorphous SiC and Si, Phys. Rev. B 75 (8) (2007).

[86] T. Morimoto, T. Ogasawara, Potential strength of Nicalon™, hi Nicalon™, and hi nicalon type S™ monofilaments of variable diameters, Compos. Appl. Sci. Manuf. 37 (3) (2006) 405–412.

[87] S. Mazerat, R. Pailler, Statistical data for the tensile properties and static fatigue of sic-based bundles, Data Brief 32 (2020), 106166.

[88] M. Braginsky, C.P. Przybyla, Simulation of crack propagation/deflection in ceramic matrix continuous fiber reinforced composites with weak interphase via the extended finite element method, Compos. Struct. 136 (2016) 538–545.

[89] W.M. Mueller, J. Moosburger-Will, M. Sause, M. Greisel, S. Horn, Quantification of crack area in ceramic matrix composites at single-fiber push-out testing and influence of pyrocarbon fiber coating thickness on interfacial fracture toughness, J. Eur. Ceram. Soc. 35 (11) (2015) 2981–2989.

[90] T. Bergs, P. Ganser, D. Fruh, J. Reisberg, Investigation of cutting mechanisms in the machining of ceramic matrix composites (CMCs), Proc. CIRP 101 (2021) 330–333, in: https://doi.org/10.1016/j.procir.2020.11.015.